# Surface Study of Volatile Organic Compounds (VOCs) Biomarkers Adsorption on Functionalized Graphene and its Application in FET Based Biosensors

Paramjot Singh

A Thesis
In the Department
of
Electrical and Computer Engineering

Presented in Partial Fulfillment of the Requirement
For the Degree of
Master of Applied Science (Electrical and Computer Engineering) at
Concordia University
Montreal, Quebec, Canada

December 2021

CONCORDIA UNIVERSITY
School of Graduate Studies

This is to certify that the thesis prepared

By: Paramjot Singh

Entitled: Surface Study of Volatile Organic Compounds (VOCs) Biomarkers Adsorption on Functionalized Graphene and its Application in FET Based Biosensors

and submitted in partial fulfillment of the requirements for the degree of

Master of Applied Science (Electrical and Computer Engineering)

complies with the regulations of the University and meets the accepted standards with respect to originality and quality.

Signed by the final examining committee:

Chair
Dr. M.Z. Kabir

Examiner
Dr. S. Jahanshahi Anbuhi (CHEM)

Examiner
Dr. M.Z. Kabir

Thesis Supervisor(s)
Dr. M. Kahrizi

Thesis Supervisor(s)

Approved by
Dr. Yousef Shayan, Chair
Department of Electrical and Computer Engineering

Dr. Mourad Debbabi, Dean
Faculty of Engineering and Computer Science

Date

# Abstract

**Surface Study of Volatile Organic Compounds (VOCs) Biomarkers Adsorption on Functionalized Graphene and its Application in FET Based Biosensors**

**Paramjot Singh, MASc.**
**Concordia University,2021**

In this work, we have designed and simulated a graphene field-effect transistor, GFET, with the purpose of developing a sensitive biosensor for methanethiol, a biomarker for bacterial infections and ethyl butyrate, a biomarker for COVID-19.

The surface of a graphene layer is engineered by manipulation of its surface structure and best cases are used as the channel of the GFET. Three methods, doping the crystal structure of graphene, decorating the surface with transition metals like Platinum and Palladium and defected graphene nanoribbons are utilized to induce the bandgap in the graphene layers.

The techniques also change the surface chemistry of the graphene by enhancing its adsorption characteristics and make binding between graphene and biomarker possible. All the physical parameters are calculated for various variants of graphene in the absence and presence of the biomarker using counterpoise energy corrected density functional theory in Quantum ATK. The device was modelled using the finite element method in COMSOL Multiphysics. Our studies show that the sensitivity of the device is affected by the structural parameters of the device, the electrical properties of the graphene, and with adsorption of the biomarkers. It was found that the devices made of graphene layers decorated with transition metals show higher sensitivities toward detecting the biomarkers compared with those made by doped graphene layers and nanoribbons.

# Acknowledgement

I would like to start by thanking “Waheguru ji” for giving me the strength and ability to understand, learn and complete this work.

I express my deep sense of gratitude to my supervisor, **Dr Mojtaba Kahrizi** for their valuable guidance, motivation, financial assistance, and full attention at all stages of my project work. Their constant encouragement, help and review of the entire work during investigation helped me to acquire and develop the skills and intricacies of good independent research. I am grateful to **Dr Parsoua A. Sohi** for guiding me in many ways during carrying out the research work. I received very useful and excellent academic training from them, which has stood in good stead while writing this Dissertation.

Also, I want to show great gratitude towards my parents, **Mr Bhupinder Singh** and **Mrs Kailash Kaur** as no words can describe their incessant encouragement and constant motivation. I also want to thank my sister **Pawanpreet Kaur** for her continuous emotional support.

I want to thank **Dr Deepkamal Kaur Randhawa**, **Dr B.C. Choudhary, Dr Himali Sarangal**, **Dr Harmandar Kaur** and **Dr Gurleen Kaur Walia** who guides me during my first step in the realm of research in my undergraduate and introduce me to computational methods used in material modelling.

This acknowledgement would be incomplete if I do not express my deep sense of gratitude to **Mrs Kavita Hastir** and **Mrs Suruchi Sharma** (my art teachers) who gives me the creativity which helps me in each and every aspect of my life.

Special thanks to my friends, **Shivam**, **Amrit**, **Tarun** and **Himanshu**.

Paramjot Singh

# Publications

**Research Paper**

1. **P. Singh**, P. A. Sohi, and M. Kahrizi, "In silico design and analysis of Pt functionalized graphene-based FET sensor for COVID-19 biomarkers: A DFT coupled FEM study," *Phys. E Low-dimensional Syst. Nanostructures*, vol. 135, no. April 2021, p. 114972, 2021, doi: 10.1016/j.physe.2021.114972.
2. **P. Singh**, P. Abedini Sohi, and M. Kahrizi, "Finite Element Modelling of Bandgap Engineered Graphene FET with the Application in Sensing Methanethiol Biomarker," *Sensors*, vol. 21, no. 2, p. 580, Jan. 2021, doi: 10.3390/s21020580.

**Conference Paper**

1. **P. Singh**, P. A. Sohi, and M. Kahrizi, "Effect of point defects in armchair graphene nanoribbons for biosensing of Methanethiol biomarkers: A DFT Study," *2021 IEEE 21st Int. Conf. Nanotechnol.*, pp. 142–145, Jul. 2021, doi: 10.1109/NANO51122.2021.9514321.

***Dedicated to my mother,***

***Mrs Kailash Kaur***

***'Kailash', named after the mountain, where Lord Shiva resides***

***act as a mountain between me and problems came in my life.***

***Thank you, Maa for everything!***

# Table of Contents

# List of Figures

# List of Table

# List of Acronyms

| | |
|---|---|
| 2Pt- graphene | 2 Pt atom per supercell decorated graphene |
| A-GNR | Armchair GNR |
| Al | Aluminium |
| AlP-GFET | Aluminium and Phosphorous doped GFET |
| AlP-Graphene | Al and P atom per supercell decorated graphene |
| BTE | Boltzmann Transport equation |
| C | Carbon |
| CBM | Conduction Band Minima |
| CP | Counterpoise corrected energy |
| DC | Direct Current |
| DFT | Density Functional Theory |
| ELISA | Enzyme-linked immunosorbent assay |
| FEM | Finite Element Method |
| FET | Field effect transistor |
| Ga | Gallium |
| GC | Gas chromatography |
| GCMS | Gas chromatography-mass spectroscopy |
| GFET | Graphene Field-effect transistor |
| GGA | Generalized Gradient approximation |
| GNR | Graphene Nanoribbon |
| GO | Graphene oxide |
| H | Hydrogen |
| In | Indium |
| LA | Longitudinal Acoustics |

| | |
|---|---|
| LBFGS | Limited memory Broyden–Fletcher–Goldfarb–Shannon algorithm |
| LCAO | Linear Combination of Atomic Orbitals |
| MP | Monkhorst-Pack grid |
| N | Nitrogen |
| O | Oxygen |
| P | Phosphorous |
| PBE | Perdew-Burke-Ernzerhof |
| Pd | Palladium |
| Pd-GFET | Palladium decorated GFET |
| Pd-graphene | Pd atom per supercell decorated graphene |
| Pt | Platinum |
| Pt-GFET | Platinum decorated GFET |
| Pt-graphene | Pt atom per supercell decorated graphene |
| RT-PCR | Reverse transcription polymerase chain reaction |
| RTA | Relaxation Time Approximation |
| S | Sulphur |
| Sb | Bismuth |
| SPME | Solid phase microextraction |
| TA | Transverse Acoustics |
| TM | Transition metal |
| VBM | Valence Band Maxima |
| VOC | Volatile Organic Compound |
| Z-GNR | Zigzag GNR |
| ZA | Out of plane Acoustics |

# Chapter1. Introduction

## 1.1 Nanomaterials based sensors

Huge development in manipulating the matter at the nanoscale with state-of-the-art devices and tools leads to the tremendous evolution of ultra-sensitive sensors [1]. Usage of nanomaterials like monolayers, nanoparticles, nanoribbons, nanorods, nanoflowers, nanowires, nanopores and others on optical, electrical, magnetic, electrochemical, and electromechanical sensors improves the analyte detection capabilities [2]–[4]. Among all the nanomaterials, two dimensional (2D) nanomaterials are widely used for electrochemical and electrical sensors like resistor and field-effect transistor-based sensors. In the mentioned sensors, nanomaterials act as a functional unit with which analyte interacts, and 2D nanomaterials exhibit a large surface for analyte interaction and improve the transducing mechanism [2]–[4].

Incorporating 2D nanomaterials like graphene, silicene, germanene, stanene, phosphorene, borophene, $MoS_2$ and others [5]–[8] in sensor manufacturing ameliorates analyte binding, detection functionalities and carrier transport properties [4]. These semiconductor/semi-metallic materials can detect a low concentration of gases and biomolecules, as their electronic and transport properties vary when exposed to a minimal number of molecules. 2D nanomaterials-based sensors are widely used in health and environmental science for routine testing because of their low cost and fast response compared to other established detection methods like Surface Plasmon Resonance (SPR), Reverse Transcription Polymerase Chain Reaction (RT-PCR), and Enzyme-Linked Immunosorbent Assay (ELISA) [2], [4], [9], [10]. Among these 2D nanomaterials, graphene shows a promising behaviour toward the sensing applications as it

exhibits high carrier mobility compared to other X-Enes like silicene, germanene and others [11]. Moreover, graphene has more facile and less costly fabrication methods with more structural stability at ambient temperature [12].

## 1.2 Graphene

In 2004, exfoliation of a monolayer of honeycomb networked carbon (C) atoms, as showing in figure 1 with C–C bond length 1.42 Å from the graphite, leads to one of the most promising materials for photonics and electronics research and industry [12], [13]. $sp^2$ hybridised carbon in this 2D material called graphene reveals remarkable electronic and mechanical properties such as tremendous mobility of charge carriers and high electric and thermal conductivities [13]. Graphene band structure exhibits linear dispersion relation, and electrons are treated as massless Dirac fermions in the lattice [14]. Owing to the fact of the linear dispersion relation, the charge

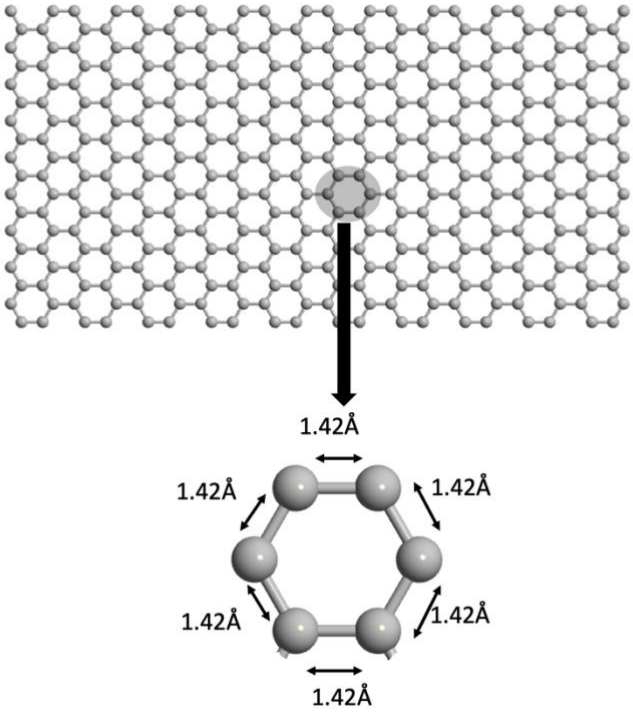


**Figure 1.1** Hexagonal structured graphene layer with bond length

carriers in graphene exhibit splendid electronic properties. Graphene has potential for many applications, such as GFET [15]–[19], photonic devices such as photodetectors [20]–[25], phototransistors [26]–[28] and mode-locked lasers [29]

As already discussed, graphene comprises the C atoms with electronic configuration, $1s^2\ 2s^2\ 2p^2$. In graphene, 2s, $2p_x$ and $2p_y$ orbital of C, hybridised to $sp^2$ covalent bonds and formed hybrid $sp^2$ wavefunction and a single σ bond between all the adjacent carbon atoms is formed [30]. The remaining $2p_z$ orbital overlap orthogonally and formed an π bond with alternative adjacent C atom. This type of σ and π bonding of C is also called the carbon-carbon conjugate bond [31]. During the bonding of atoms, the more the overlapping of the wavefunction, the more energy will be released, and the system will be more stable. In $sp^2$ hybridisation, the most stable structure occurs when the hybrid bonds are 120 degrees apart from each other in the same plane which is orthogonal to the plane of $2p_z$ orbital [30]. This systematic spatial occurrence bond in $sp^2$ hybridisation results in the hexagonal/honeycomb shape of graphene (figure 2(a)). This structure of graphene is also referring as Clar's structure in the consequent chapters [31]. Due to this special hexagonal atomic arrangement, graphene does not form a primitive unit cell. Instead, it has a triangular unit cell shown in figure 2(a) contain two basis points with lattice vector given in (1) [30]

$$\overrightarrow{a_1} = \frac{a}{2}\left(3, \sqrt{3}\right) \text{ and } \overrightarrow{a_2} = \frac{a}{2}\left(3, -\sqrt{3}\right) \tag{1.1}$$

Where $\overrightarrow{a_1}$ and $\overrightarrow{a_2}$ are lattice vector and a is the bond length between C atoms.

The Brillouin zone of reciprocal lattice of graphene is similar to its unit cell, i.e., triangular, as present in figure 2(b) with lattice vector given in (2) [31]

$$\overrightarrow{b_1} = \frac{2p}{3a}\left(2, \sqrt{3}\right) \text{ and } \overrightarrow{b_1} = \frac{2p}{3a}\left(2, -\sqrt{3}\right) \quad (1.2)$$

Where $\overrightarrow{b_1}$ and $\overrightarrow{b_2}$ are reciprocal space lattice vector.

The K and K' are the main two points in the Brillouin zone where high symmetric Dirac cones are formed, and their wave vectors are given in (3) [30]

$$\vec{K} = \left(\frac{2p}{3a}, \frac{2p}{3\sqrt{3}a}\right) \text{ and } \overrightarrow{K'} = \left(\frac{2p}{3a}, \frac{2p}{3\sqrt{3}a}\right) \quad (1.3)$$

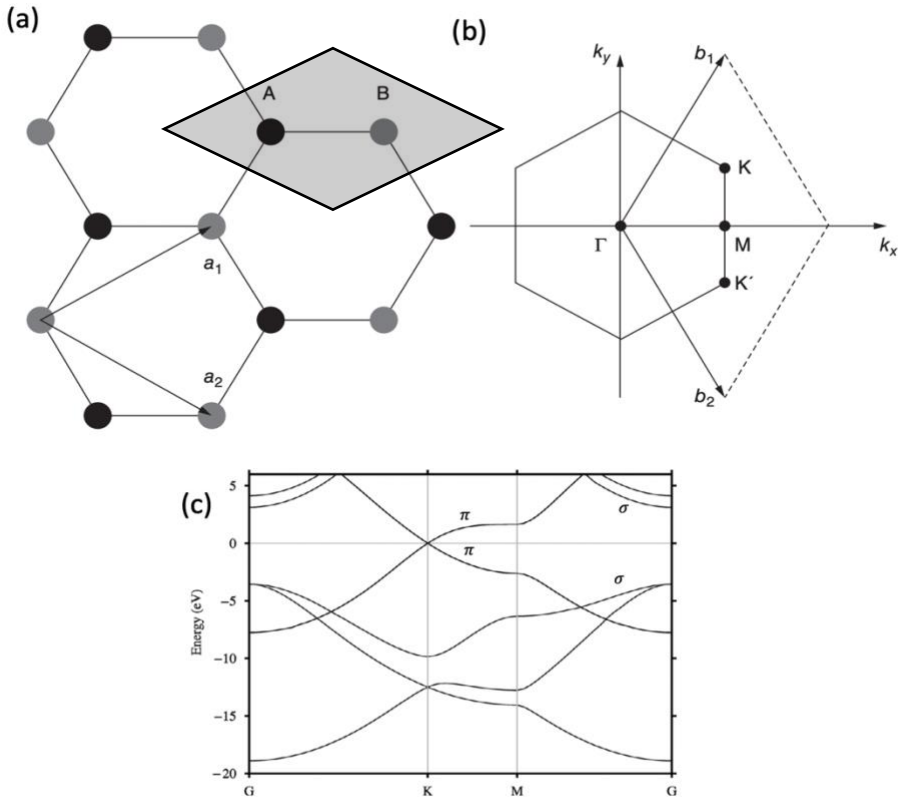


**Figure 1.2** (a) Graphene structure with lattice vectors (b) Brillouin Zone of Graphene with lattice vector (c) Band structure of graphene [29]

Graphene exhibits a very peculiar electronic structure. Figure 2 (c) illustrates the band structure of graphene. In the figure, σ bond states form the bands quite away from the Fermi level (depicted by 0 in the figure) with a large bandgap [31]. π bond states form a band between the σ bond states that meet with each other at Fermi energy level and form a very symmetrical Dirac cone at K point of Brillouin zone [30]. Due to the formation of these symmetrical cones, the simplified dispersion relation of graphene is linear around the fermi level, as given in (4) [32]

$$E = \hbar \, v_f \, k \tag{1.4}$$

Here, E is energy eigenvalue, $\hbar$ is modified planks constant, $v_f$ is fermi velocity, and k is wave vector.

Due to linear dispersion relation in vicinity of Fermi level electrons of graphene are considered massless fermions [32]. Although the valence band and conduction band are meeting at the K point, valence band is filled, and the conduction band is empty because the Fermi level exists at the exact point where both bands coincide with each other [31]. Therefore, graphene is considered a semi-metallic or zero bandgap semiconductor.

## 1.3 Bandgap engineering of graphene

Semi metallicity is the property that conceals graphene's functionalities and limits its applications, especially for semiconductor technology. To overcome this limitation, this hexagonally structured material is transformed into a semiconductor through various bandgap engineering methods discuss below:

### 1.3.1 Graphene nanoribbon

Creating quantum confinement by constraining the graphene in one dimension leads to the formation of the graphene nanoribbon (GNR) [33], [34]. The atomic configuration at the edge of the GNR is classified into armchair GNR (A-GNR) and zigzag GNR (Z-GNR), as shown in figure 3. Under nonmagnetic conditions, Z-GNR is metallic [33]. However, A-GNR exhibit semiconducting properties along with the parabolic dispersion relation. A-GNR exhibited width dependent bandgap and was grouped into three families, W= 3p, 3p+1 and 3p+2, where W is the number of atoms associated with the width of the A-GNR and p is the positive integer. Studies reveal that the 3p and 3p+1 classes of A-GNR show semiconducting properties [35] [36]. In all configurations, the bandgap is inversely proportional to the W of the A-GNR [35]. The existence of dangling bonds makes the edges of the structure highly reactive and chemically unstable. Therefore, edges of the GNR are passivated with different elements like hydrogen [37], halogens (F, Br) [38], [39] , nitrogen [40], sulphur [41] and oxidising agents (OH and O) [42]. Hydrogen is the most common passivation agent and is widely explored in terms of electronic, magnetic, surface and transport properties [37].

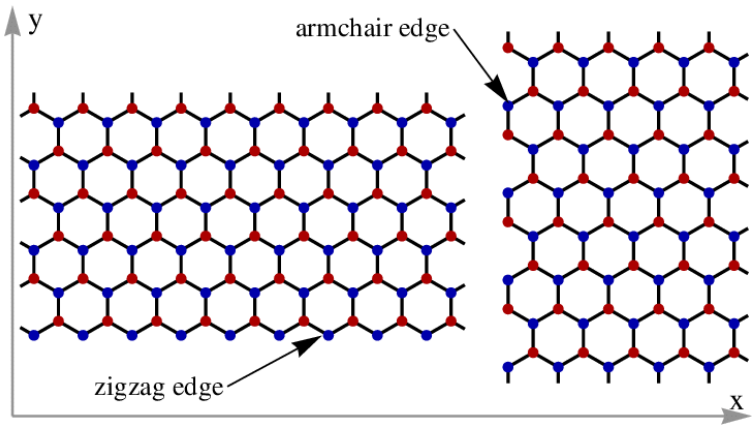


**Figure 1.3** Armchair and zigzag edges of GNR [33]

### 1.3.2 Straintronics

Mechanical strain varies the electronic properties of graphene. Strain can be applied via various techniques, by bending the substrate material and through lattice mismatching with substrate materials like Silicon Carbide (SiC) and others. With the increment of uniaxial strain on the graphene, the $\pi$ band start moving away from the Fermi level, but the $\sigma$ band in the conduction band start moving towards the vicinity of the Fermi level [43]. Therefore, a specific amount of uniaxial strain on the zigzag graphene layer gives rise to a bandgap in the graphene [44]. The uniaxial strain should be large enough to make $\pi$ band away from the Fermi level but small enough to prevent coinciding $\sigma$ band with Fermi level [43].

Moreover, it found out that strain also affects the density of states and the work function of the graphene. The density of states near the Fermi level of the strained graphene increases abruptly with an increment of strain. Similarly, work function increases as the strain on the graphene increases. Applying uniaxial strain makes the quasiparticles heavy in the applied strain direction [43]. The isotropic strain does not affect the bandgap of the graphene layers.

### 1.3.3 Doping

Doping is another method to change the electronic structure of graphene. Doping is broadly classified into three types (1) n-type (2), p-type (3) compensated doping. In n-type doping, the impurity atoms like N, P, As, and Sb are one electron-rich than the C atom, and in p-type doping, impurity atom-like B, Al, Ga and In is one electron deficient. Besides changing the position of the Fermi level, doping generates the bandgap in the graphene [45]. In n-type doping of graphene, the amount doping leads to opening of bandgap in graphene makes the Fermi level reach above the conduction band maxima, resulting in the formation of non-degenerate n-type

semiconductors that do not have much use in semiconductor device fabrication [45]. Similarly, p-type doping results in the formation of a non-degenerate p-type semiconductor.

The compensation doping, i.e., p-type and n-type dopant involvement in graphene, leads to the opening of the graphene bandgap without shifting the Fermi level much above or below the conduction band maxima and valence band minima, respectively [46].

### 1.3.4 Functionalization

Functionalization is an effective and established technique to mutate the dispersion relation and open the bandgap [47]. In functionalization, the structure of the graphene is not distorted as done in the case of doping; instead, a dispersed layer of the foreign element can be biomolecules like DNA or chemical agents like metal nanoparticles, halogen atoms and others are formed. Functionalization also serves the purpose of binding target sensing molecules to the device. So, this type of bandgap engineering method serves a dual purpose for sensor devices. Not every Functionalization agent can transmute graphene into the semiconductor [48]. The Functionalization agent, which forms covalent bonding with the graphene, has strong capabilities to open the bandgap. Group 10 transition metals (TMs) like platinum (Pt), halogens, aryl, hydroxyl surface decoration and others are used as a Functionalizing agent for graphene for sensing application [48]–[50].

## 1.4 Graphene sensors

Due to the flexible structure, large surface area, superior electrical, mechanical, and optical properties, graphene is utilised as a part of highly sensitive sensors, [51] although its chemical inertness and zero bandgap hinder the sensing capabilities. To improve the above properties, the

graphene surface needs to be Functionalized/doped. Functionalization/doping elevates the reactivity of graphene and makes it sensitive toward selective molecules. Functionalized graphene sensors has been reported to sense folic acid [52], *E-coli* [53], glucose [54] , DNA [55], dopamine [56], methanethiol biomarker [57] and others. Schedin et al. [58] developed the first graphene-based gas sensor. The sensor works based on the change in the hall resistance of the graphene layer as the local carrier concentration varies due to the adsorption of $NO_2$ molecules on the surface. After that, researchers work extensively on graphene and its derivatives for sensory activities based on piezoelectric effects, optical effects, surface phenomenon and others.

## 1.5 Volatile Organic Compounds biomarkers detection technique

Humans breathe composed of various elements, but when the human body suffers from any disease, some specific VOCs start forming or their level increases abruptly in a breath [59]. If a device can identify the associated VOCs biomarkers, the disease can be identified. Therefore, it is a novel, rapid and non-invasive technique of detection. For this technique, the methods like solid-phase microextraction (SPME) methods coupled with gas chromatography (GC) or gas chromatography-mass spectroscopy (GCMS) are widely used [60], [61]. Some of the VOCs biomarkers used in this research work are discussed below:

Methanethiol is volatile organo-sulphur material considered a VOC biomarker for diseases caused by microorganisms like *helicobacter pylori bacteria (H. pylori*) and *porphyromonas gingivalis (P. Gingivalis) phylum Bacteroidetes* [57].

Ethyl butyrate, a breath-born VOC biomarker for COVID-19. Comprehensive quantitative exhale breath analysis of virus-infected, non-infected and other lung-related diseases patients confirm that this biomarker serves as an indicator for this disease [62].

## 1.6 Objective of research

Objectives of this research work are:

- To study the methodologies (via DFT) for opening the bandgap of graphene monolayer via Transition metal decoration, III-V group element co-doping and by creating quantum confinement via forming graphene nanoribbon and make material compactible for semiconductor process technology.
- To study the interaction (via DFT) between the different VOC biomarker like methanethiol and ethyl butyrate adsorption on different types of bandgaps engineered graphene nanostructures discussed above. To get intuitive perception about using bandgap engineering sites on graphene as a binding site for biomarker molecules.
- To design a GFET biosensor micro-device (via FEM) for detecting VOC biomarkers of bacterial and viral infection, an alternative approach developed for sensing VOCs. Where, bandgap engineered graphene used as channel of device.
- This research work gives a simulation method to check the sensitivity GFET sensor for particular type of VOCs, which involves interaction study of channel of device with molecules via DFT methods and device properties calculation using FEM via COMSOL Multiphysics

## 1.7 Organization of thesis

There is eight-chapter in the thesis, which starts with

- Chapter 1, which gives an introduction to nanomaterial-based sensors and the fundamental chemistry and physics of graphene which includes its bonding-hybridization pattern and band structure formation. Moreover, the different method used in literature

for the opening of graphene bandgap is explained with the use of graphene in sensors and a brief introduction to volatile organic compounds-based sensing technique. The chapter ends with the scope and organisation of this research work.

- Chapter 2 gives the review of graphene-based biosensing techniques. It starts with the dual functionalities of functionalization of graphene and describes different types of Functionalization that can be performed on graphene. Afterwards, different graphene-based biosensing techniques are discussed, including electrochemical, surface plasmon resonance and field effects transistor.
- In chapter 3, the computational approach used in the research work is described, starting with a brief introduction to density functional theory and how it works. Afterwards, the parameters and approximations used in the density functional theory calculations are explained. Additional calculations or simulation prior to basic density functional theory calculation is mentioned like adsorption energy calculation, the effective density of states calculation mobility calculations and others. The chapter ends with a brief mathematical introduction to drift-diffusion formalism used in device study.
- Chapter 4 describes the different bandgap engineering methods used in this research work like compensating doping, transition metal atoms decoration and pristine/defective graphene nanoribbon formation. Each structure's stability is checked via geometry optimization. The chapter also explains how these methods affect the clar's structure of graphene.
- Chapter 5 explores the interaction between the biomarker molecules and the bandgap engineered graphene via adsorption energy and Mullikan bond population analysis. Only those cases are considered which forms strong interaction with any biomarker.

- Chapter 6 is based on the electronic properties calculation of the structures mentioned in chapters 4 and 5. This chapter gives a comprehensive view of electronic properties used in semiconductor device physics and shows how variation occur in electronic properties after adsorption of the biomarker molecules.
- Chapter 7 is based on device modelling using bandgap engineered graphene structure modelled in chapters 4 and 5, and its characterization. Moreover, it also describes the variation of the current characteristics after the adsorption of biomarker molecules. This variation in current characteristics is used to sense the biomarker molecule. The chapter ends with sensitivity calculation of the modelled sensor with different biomarkers and concentrations.
- Chapter 8 give the conclusion and future scope of this research work.

# Chapter 2. Graphene-Based Biosensing Techniques

## 2.1 Graphene functionalization

The versatile nature and extraordinary electronic properties of graphene mentioned in chapter 1 make it an ideal candidate for biosensing application. For biosensing applications, graphene requires Functionalization. Functionalization can be used for bandgap engineering to develop a device based on semiconductor process technology, as discussed in chapter 1, but it also improves the selectivity and binding of the target biomolecule or biomarker molecule. Various types of Functionalization, covalent and non-covalent can be performed on the graphene layers.

### 2.1.1 Covalent functionalization

In the covalent type of functionalization, a covalent bond exists between the Functionalizing agent and graphene, affecting the carbon-carbon conjugate bond. Covalent functionalization involves binding with organic molecules, halogens, hydrogen, and others. Covalently attached hydrogen with graphene is called graphene [48]. In organic molecules functionalization, there are two common routes in which covalent functionalization can be performed on graphene [48]. First is when the free radical is attached with the C-C bond of the graphene, which involves the $\pi$ bond. The second is the formation of graphene oxide (GO) via oxidation and then involve bonding between the oxygen (O) of GO and the functional group.

### 2.1.2 Noncovalent functionalization

The non-covalent type of functionalization exploits the stacking properties of graphene to form graphite. In graphite, graphene shows π-π interaction with each other. If this interaction can exist between the functionalizing agent and the graphene, non-covalent Functionalization occurs [48]. Various types of detection methods for biosensors are developed using the functionalized/non-functionalized graphene material discuss in the following subsequent paragraphs

## 2.2 Graphene modified electrode electrochemical biosensor

Electrochemical sensors are based on redox or oxidation reaction occurrence and its effect on the electrical signal of the system. Functionalized graphene is used to modify the working/ sensing electrode of the system to improve the selective and sensitivity of the system [63], [64]. This improves the diffusion of the target molecules and changes the system's electrical signal, which is used as a sensing parameter. Graphene-based electrochemical sensors are reported for sensing dengue virus, Avian influenza virus *H7*, Influenza A virus, cardiovascular diseases, hormones, celiac disease, and DNA [65].

## 2.3 Graphene/metallic thin film-based surface plasmon resonance biosensor

The surface plasmon resonance sensor is based on the change in the resonance peak of surface plasmon polaritons with respect to incident angle or wavelength [66]. These sensors are based on graphene/metallic thin layer coupled with prism via different coupling techniques like Otto and Kretschmann coupling or optical fiber and a layer analyte on top of graphene/ metallic thin film [67]. When light suffered total internal reflection from graphene/metallic thin film and SPR occurs at the resonance frequency [68]. For different analytes, the resonance frequency changes.

The role of graphene is to bind the selective analyte with a metallic thin film. Graphene/ metallic thin film-based SPR is reported for sensing human immunoglobulin G, DNA hybridisation, formalin, and biomarkers of breast cancer [69]–[72].

## 2.4 Graphene field-effect transistor biosensors

The contemporary graphene sensor technology is based chiefly on GFETs. There are two types of GFET sensors discussed in the subsequent paragraphs

### 2.4.1 Dielectric modulated GFET sensors

In Dielectric modulated GFET sensors, a dual/ single gated GFET is used with a cavity in the dielectric layer of the gate [73]. That cavity is used to fill up with biomolecules or biomarkers, as shown in figure 4. This type of sensor is based on the dielectric properties of the biomolecules. Each biomolecule has a different dielectric constant and consequently have its current characteristics [74]. It is reported that, for dielectric modulated FET sensors, the cavity along the source side is impactful, whereas the cavity on the drain side does not have a significant impact on the sensitivity of the sensors [75][76]. The charge of the biomolecule also affects the sensing property of the device. In the case of negatively charged biomolecules, the charge effect on the sensitivity overcomes the dielectric constant effect on the sensitivity. Moreover, this type of sensor functionalization is not a mandatory step for fabrication because analytes do not come in contact with the graphene layer. It is a label-free detection technique [75].

The major drawback of this type of sensor is that it only accounts for one property of material for sensing, i.e., dielectric constant. Many neutral biomolecules or biomarkers possess the same

dielectric constant or with a minor change. In that case, the sensor becomes ineffective to sense those molecules. Therefore, backend gate FET sensor structure is preferred.

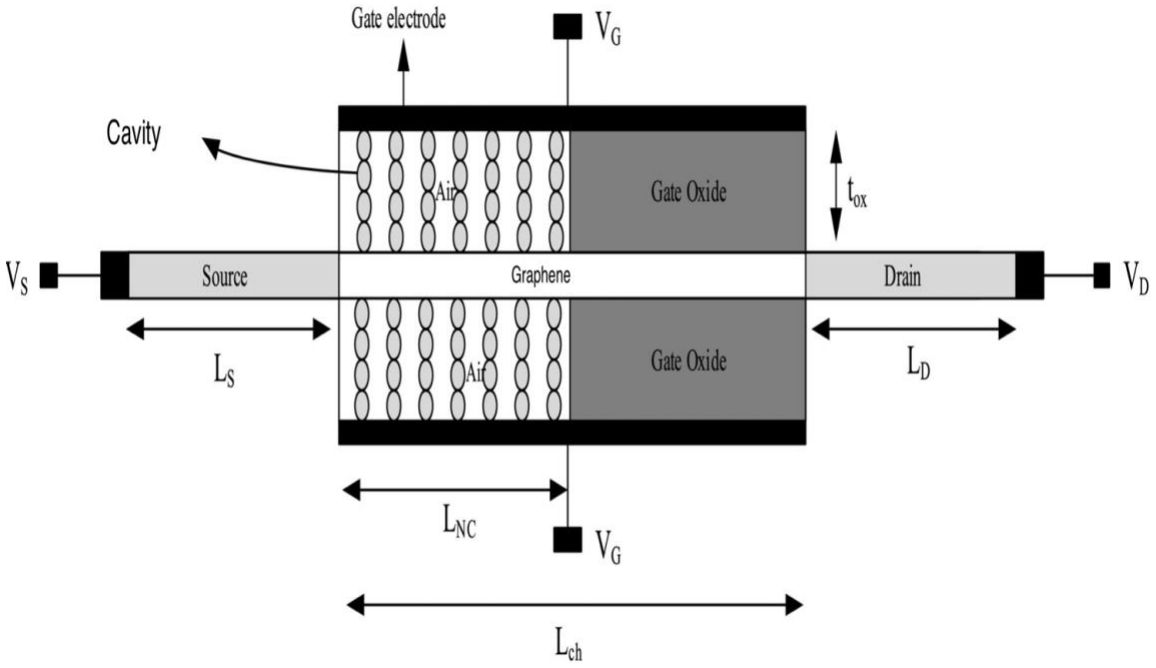


**Figure 2.1** Dielectric modulated GFET sensor with dual gates [72].

### 2.4.2 Channel modulated GFET sensors

The Present GFET sensor technology is based on channel modulated GFETs as shown in figure 5. A GFET consists of a graphene layer as the transistor channel lies on a semiconductor/metallic substrate coated with the dielectric layer. The transistor operates using two ohmic contacts to the graphene channel, the source, the drain, and a third contact to the gate, which controls the charge transfer characteristics of the graphene [57]. The principle of operation of channel modulated GFET sensors relies on the fact that the surrounding environment affects the electrical properties of graphene and consequently affects the I-V characteristics of the device. For this reason, usually, a back gate structure is preferred for sensing applications to allow the exposure of the graphene layer to the sensing targets. Channel modulated GFETs are reported for sensing several

chemical/biomolecules such as OH ions, monosodium L-glutamate, *E-coli*, ethanol, glucose, hydrogen gas, exosomes, nitrogen-based gases [57]

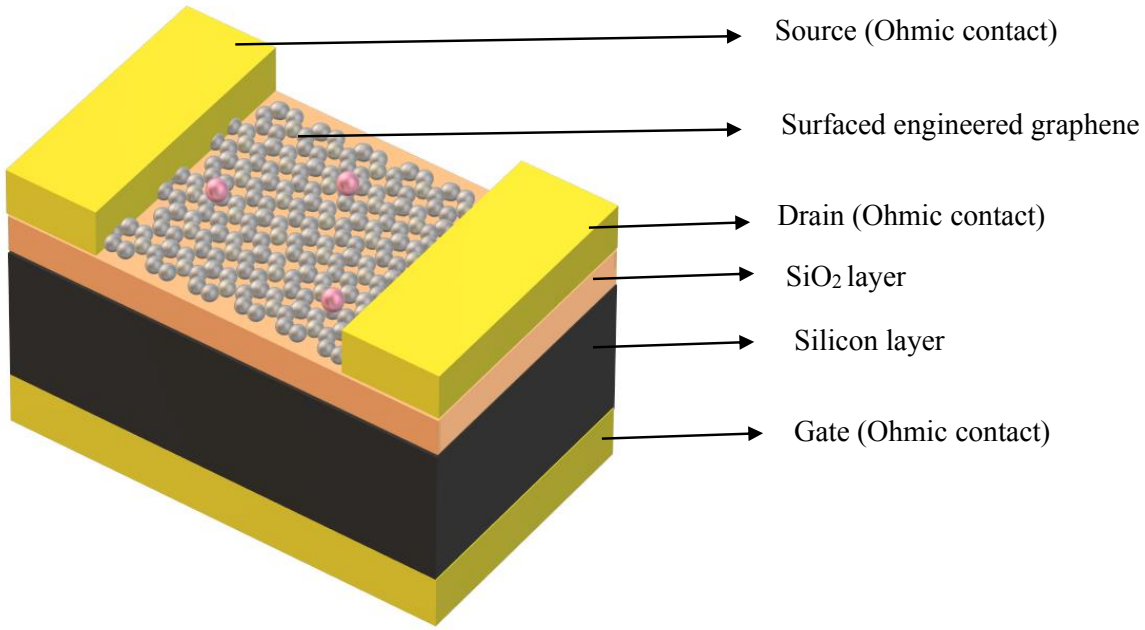


**Figure 2.2** Channel Modulated GFET[77]

Figure 6 illustrates a typical ambipolar I-V characteristic of a GFET. Unlike semiconductor-based FETs with unipolar characteristics, these transistors do not show an off-state. Instead, when sweeping the gate from negative to positive voltages, the charge carriers in the channel are continuously modulated from holes to electrons. At the transition point (Dirac point) known as charge neutrality, the hole carrier density matches the electron carrier density, and the graphene conductance reaches its minimum value at a gate voltage, $V_n$.

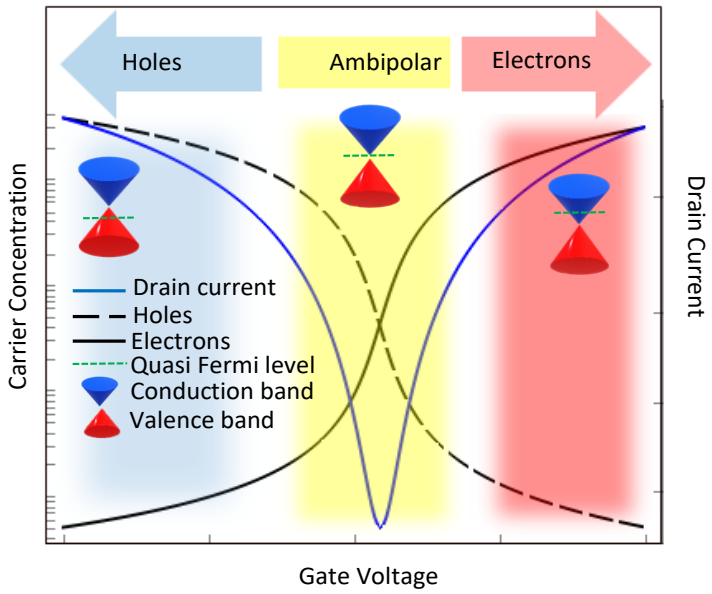


**Figure 2.3** I-V characteristics of GFET device shows unipolar and ambipolar regions according to the carrier concentrations in the channel [77].

This ambipolar behaviour is attributed to the graphene band structure. As it is shown in figure 6 by variation of the charge carrier type and concentration (controlled with an external electric field sweeping the gate voltage), the quasi-Fermi level is driven from the valence band to the conduction band. The conductivity also increases with increasing the concentrations of charged carriers. The minimum current density is observed when the quasi-Fermi level crosses the Dirac point of the band structure [57].

As graphene exposure to the biomarkers under investigation is linked to the alternation of the Dirac point of the band structure, the $V_n$ point of the I-V characteristics is used to detect the targets.

Now onwards in this thesis, the GFET sensor refers to the channel modulated GFET sensor.

# Chapter 3. Computational Methodology

The computational methodology used in this research work is a combination of DFT and FEM. DFT via Quantum ATK is used to calculate the Electronics properties of the bandgap engineered graphene with and without interaction of biomarker molecule. Electronic properties such as band structure, mobility, the effective density of states, effective masses, work function and electron affinity are calculated using DFT. Bonding analysis like Adsorption energy and Mullikan population analysis is also calculated by DFT to analyze the surface phenomena on all variants of graphene with or without adsorption of biomarkers.

The calculated electronic properties parameters are used to design and simulate the GFET devices using COMSOL Multiphysics which is based on FEM analysis.

Section 3.1 gives a brief introduction to DFT, approximations and other parameters used in the simulation. Section 3.2 to 3.4 elaborate the additional calculation or simulation coupled with DFT to calculate the respective electronic properties. Section 3.5 explains the drift-diffusion formalism of the GFET device used in COMSOL Multiphysics simulations.

## 3.1 Density Functional Theory

DFT is based on the Hohenberg-Kohn theorem [78] which relates the external potential of a system that contains electrons with its ground-state electron density and Kohn-Sham equations [79]. To be more precise, DFT expresses the effective potentials of the system as functional of electron density than wavefunction.

The Kohn Sham equation is given in (5)

$$\left[\frac{-\hbar^2}{2\mathrm{m}}\nabla^2 + V_{eff}[\mathrm{n(r)}]\right]\Phi_\mathrm{i} = \mathrm{E}\Phi_\mathrm{i} \tag{3.1}$$

Here, $\widehat{\mathrm{H}}$ is Kohn Sham Hamiltonian and given as $\frac{-\hbar^2}{2\mathrm{m}}\nabla^2 + V_{eff}[\mathrm{n(r)}]$, $\frac{-\hbar^2}{2\mathrm{m}}\nabla^2$ the term expresses the kinetic energy of the system which is a linear combination of orbitals without considering any interaction occur due to other electronic particles, all these interactions are move under effective potential calculations. n(r) is electron density in the system and expressed as $\mathrm{n(r)} = \sum|\Phi_\mathrm{i}|^2$, $\Phi_\mathrm{i}$ is the wavefunction, E is energy eigenvalue, $V_{eff}[\mathrm{n(r)}]$ counts the potential energy that emerges from different types of interaction between the particles. $V_{eff}[\mathrm{n(r)}]$ have different type of potential which are expressed as follow

$$V_{eff}[\mathrm{n(r)}] = V_H[\mathrm{n(r)}] + V_{xc}[\mathrm{n(r)}] + V_{ext} \tag{3.2}$$

Here $V_H[\mathrm{n}]$ is Hartree potential, $V_{xc}[\mathrm{n}]$ is exchange-correlation and $V_{ext}$ is external potential. Hartree potential counts the mean electrostatic interaction between the electronic particles, exchange-correlation counts quantum mechanical interaction contribution due to electronic particles discussed above and external potential express the pseudopotential in this research which counts the electrostatic potential due to core electrons of the atoms. The above DFT calculation method is illustrated in form of a flowchart in figure 7.

In this research work, the Fermi Dirac distribution function is used as an occupational function for electron density calculation, which is a central property in Hartree potential calculation. Generalized gradient approximation (GGA) with Perdew-Burke-Ernzerhof (PBE) [80] is used

for exchange-correlation potential calculations. The core electrons of atoms are expressed in terms of the pseudo dojo pseudopotential set, which describes the external potential in the effective potential of Kohn-Sham Hamiltonian. The eigenfunction, of the Kohn Sham equation, is expressed in terms of a Linear combination of atomic orbitals (LCAO) basis sets.

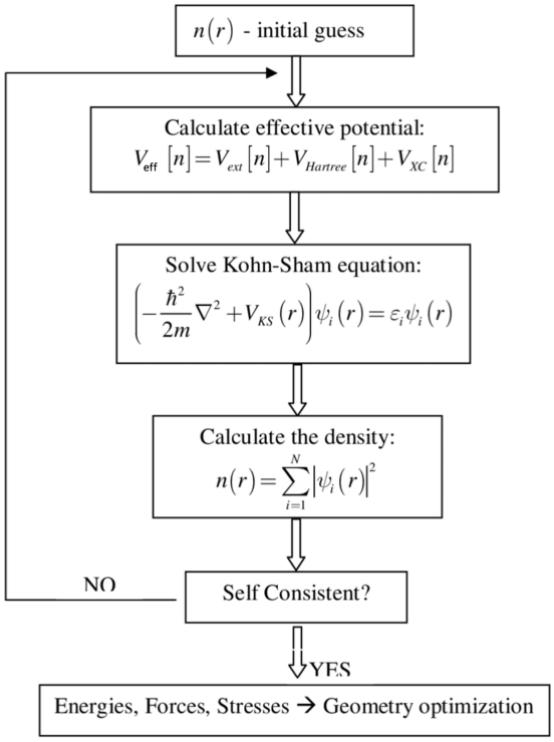


**Figure 3.1** The flowchart of Working of DFT.

Each Structure considered for DFT calculations are fully relaxed using geometry optimization through Limited memory Broyden–Fletcher–Goldfarb–Shannon algorithm (LBFGS) with 0.0001 eV/Å force tolerance and 0.1 GPa stress error tolerance. The k point sampling of Brillouin zone is set at 9×9×1 using Monkhorst-Pack grid (MP) for electronic properties, surface properties and geometry optimization except for the density of states for which it is 33×33×1 because dense k mesh gives more accurate results for density of states [81]. For all Calculations, 5×5×1 supercell of graphene or its complexes is considered.

For work function and electron affinity calculation, the Dirichlet boundary conditions are used in [001] direction and Neumann boundaries conditions are used at [$00\bar{1}$] direction of the supercell. which mimics the far away vacuum condition.

DFT calculations are used for the electronic and surface properties evaluation through Quantum ATK/2019.12.

## 3.2 Adsorption Energy

The adsorption/binding energy measures the association and dissociation of the analyte with the material and can be found from

$$E_{AD} = E_{HM+A} - E_{HM} - E_A \quad (3.3)$$

Where, $E_{AD}$ is adsorption energy or binding energy between analyte and material, $E_{HM+A}$ is the total energy of the analyte adsorbed complex, $E_{HM}$ is the total energy of the material and $E_A$ is the total energy of the biomarker. When the total energy of two interacting systems is calculated, there is overlapping of basis orbitals which results in an artificial interaction between the two systems. To eliminate the error counterpoise energy ($E_{CP}$) is added to $E_{AD}$, $E_{AD+CP} = E_{AD} + E_{CP}$ where, $E_{AD+CP}$ is the corrected total adsorption energy

## 3.3 Effective density of states

Effective density of states is used as a mathematical expression which is calculated to simplify the carrier concentration expression in the semiconductors. The expression $N_c$ and $N_v$ are given below [82]

$$N_c = 2\left(\frac{2\pi\, m_n^{DOS} k\, T}{h^2}\right) \tag{3.4}$$

$$N_v = 2\left(\frac{2\pi\, m_p^{DOS} k\, T}{h^2}\right) \tag{3.5}$$

Here, $m_n^{DOS}$ and $m_p^{DOS}$ are the effective density of state mass which is given as [83]

$$m^{DOS} = \Delta^{\frac{2}{3}} (m_l\, m_{t1} m_{t2})^{\frac{1}{3}} \tag{3.6}$$

Here, $\Delta$ is the number of valleys opposite to each other (valley degeneracy), $m_l$ is longitudinal effective mass, $m_{t1}$ and $m_{t2}$ is transverse effective masses. When these masses are calculated with corresponding to CBM, it is $m_n^{DOS}$ and when calculated correspond to VBM, it is $m_p^{DOS}$. The longitudinal mass is effective mass which is calculated along the direction of bending of CBM or VBM and the transverse is the effective mass which is calculated along with all two-perpendicular directions to the direction of band bending. $m_l$, $m_{t1}$ and $m_{t2}$ can be calculated from the band structure of the material as shown

$$m = \frac{\hbar^2}{(2d)}\, m_e \tag{3.7}$$

Here, $m_e$ is rest mass of electron and $d = \left.\frac{\partial^2 E}{\partial k^2}\right|_{k=k_o}$, E is energy eigenvalue at particular k point $k_o$.

## 3.4 Mobility

When an external electric field ($E_{ext}$) is applied to the semiconductor or metal, the carrier starts moving with the velocity ($v_d$). The external electric field is directly proportional to the velocity with mobility ($\mu$) as a constant of proportionality and it signifies the ease with which the carriers move in the material. In this study semi-classical approach is used to determine the mobility which is given [84], [85]

$$\mu = -2e\frac{\sum_{kn} v_{kn}^2 \frac{\partial f_{kn}^0}{\partial \epsilon_{kn}} \tau_{kn}}{\sum_{kn} f_{kn}^0} \tag{3.8}$$

Similarly, the mobility of holes can be calculated by replacing the occupational function $f_{kn}^0$ with 1-$f_{kn}^0$.Here, k and n correspond to k point and band index, v is the velocity of the electron. $f_{kn}^0$ is an occupational function at equilibrium which is Fermi function and $\tau_{kn}$ is relaxation time which is determined by 13 [84] and obtained from Boltzmann transport equation with relaxation time approximation and low electric field condition.

$$\frac{1}{\tau_{kn}} = \sum_{k'n'} \frac{\left(1-f_{k'n'}^0\right)}{\left(1-f_{kn}^0\right)} (1 - \cos(\theta_{kk'}))\, S_{kk'}^{nn'} \tag{3.9}$$

Here, k and n denote k point and band index of one quantum state and k' and n' denote it for other quantum states, $S_{kk'}^{nn'}$ is scattering parameter which elaborates the scattering events that occurred during transport and using Fermi golden rule it is elaborated in 14[84] and $\cos(\theta_{kk'})$ is scattering angle and is defined in 14

$$S_{kk'}^{nn'} = \frac{2\pi}{\hbar} |g_{kk'}^{\lambda nn'}|^2 [\, n_q^{\lambda} \delta(\epsilon_{k'n'} - \epsilon_{kn} - \hbar\omega_{q\lambda}) \delta_{k',k+q} + (1 + n_q^{\lambda} \delta(\epsilon_{k'n'} - \epsilon_{kn} - \hbar\omega_{q\lambda}) \delta_{k',k+q}] \quad (3.10)$$

Here, $|g_{kk'}^{\lambda nn'}|$ is electron-phonon coupling matrix and given as $|g_{kk'}^{\lambda nn'}| = \langle n'\, k'|\delta H_{q\lambda}|nk\rangle$, $\delta H_{q\lambda}$ is the perturbed Hamiltonian due to phonon electron interaction occur in the lattice. q and λ describe the quantum state of the phonon where q denotes the momentum of the phonon and λ denotes the branch index of the phonon band structure. First-term in the square bracket explains phonon absorption in the collision phenomena and the second denotes the emission phenomena. The addition of 1 in the second term elaborates the spontaneous emission of phonon.

$$\cos(\theta_{kk'}) = \frac{v_{kn}\, v_{k'n'}}{|v_{kn}||v_{k'n'}|} \quad (3.11)$$

Here, $v_{kn}$ denotes the electron velocity corresponds to quantum state with k as k point of reciprocal space and n as band index.

### 3.5 Drift Diffusion formalism

The carrier transport behaviour inside the semiconductor material that is the graphene layer of the FET is governed by 16 and 17 [86]

$$J_n = qn\mu_n \nabla E_c + \mu_n K_B T \nabla n + qnD_{n,th} \nabla\, In(T) \quad (3.12)$$

$$J_p = qn\mu_p \nabla E_v + \mu_p K_B T \nabla p + qnD_{p,th} \nabla\, In(T) \quad (3.13)$$

Here $J_n$ and $J_p$ is the current density due to holes and electrons, $\mu_n$ and $\mu_p$ are mobility of the electrons and holes, $K_B$ is Boltzmann constant, $\nabla E_c = -(V + \chi_0)$ and $\nabla E_v = -(V + \chi_0 + E_{g0})$, V is the potential, $\chi_0$ electron affinity at equilibrium, $E_{g0}$ is bandgap at equilibruim.

The charge conservation condition is implied on the oxide layer which signifies that there is no charge carrier movement from the oxide layer to the semiconductor material which means, $n.J_n = 0$ and $p.J_p = 0$ at the boundaries of the insulator layer with semiconductor. Metal contact attaches to the graphene and silicon is ohmic in nature and exhibits ohmic boundary conditions According to which, $n_{eq} - p_{eq} + N_a^- - N_d^+ = 0$. Here, $n_{eq}$ and $p_{eq}$ are equilibrium carrier concentrations are given in 18 and 19 [86] where $Na^-$ and $N_d^+$ are ionized electrons and holes of the material.

$$n_{eq} = \frac{1}{2}(N_d^+ - N_a^-)^2 + \frac{1}{2}\sqrt{(N_d^+ - N_a^-)^2 + 4\gamma_n\gamma_p n_i^2} \tag{3.14}$$

$$p_{eq} = \frac{1}{2}(N_d^+ - N_a^-)^2 + \frac{1}{2}\sqrt{(N_d^+ - N_a^-)^2 + 4\gamma_n\gamma_p n_i^2} \tag{3.15}$$

Here, $\gamma_n$ and $\gamma_p$ are given in 20 and 21

$$\gamma_n = \frac{F_{1/2}\left(\frac{E_{fn}-E_c}{K_B T}\right)}{\exp\left(\frac{E_{fn}-E_c}{K_B T}\right)} \tag{3.16}$$

$$\gamma_p = \frac{F_{1/2}\left(\frac{E_v-E_{fp}}{K_B T}\right)}{\exp\left(\frac{E_v-E_{fp}}{K_B T}\right)} \tag{3.17}$$

Here, $F_{1/2}$ is Fermi integral of order ½ , $E_{fp}$ and $E_{fn}$ are the quasi-Fermi level of electrons and holes. The potential across the metal contact is given by 22

$$V = V_0 + V_{eq} \tag{3.18}$$

Here, $V_0$ is externally applied potential to the device and $V_{eq}$ is given in 23 [86]

$$V_{eq} = V_0 - \chi - \frac{E_g}{2e} + \frac{K_B T}{e}\left(\log\left(\frac{n_{eq}}{\gamma_n n_i}\right) + \frac{1}{2}\log\left(\frac{N_v}{N_c}\right)\right) \tag{3.19}$$

# Chapter 4. Bandgap Engineering Methods of Graphene

## 4.1 Compensating doping

As discussed in Chapter 1 compensating doping is, in which n-type and p-type dopant involves. Figure 8(a) illustrates the atomic structure of the Al-P doped graphene lattice. Optimization is performed to achieve the lowest energy structure and therefore, the most stable atomic configuration. The zoomed-in areas in the figure present the calculated Al—C, P—C and C—C bond lengths of a ground-state optimal structure.

In the proposed structure, P with one extra electron than C acts as an n-type impurity by incorporating one electron per $nm^2$ to the graphene lattice. Whereas Al is one electron-deficient and acts as a p-type impurity by incorporating one hole per $nm^2$ to the lattice structure. Figure 8(b) illustrates the doped graphene structure with semi-infinite extension in [100] and [010] directions considered for energy-band structure calculations.

The same analyzes are also performed for B-N and Ga-As dopants. Each dopant atom is linked with three C atoms and forms different bond lengths. These bond lengths along with induced bandgap are summarized in Table 1. All the DFT calculations are performed on the same concentration of dopants of one pair of donor-acceptor per $nm^2$. It is found that the Ga-As pair has induced maximum bandgap as compared to other dopants.

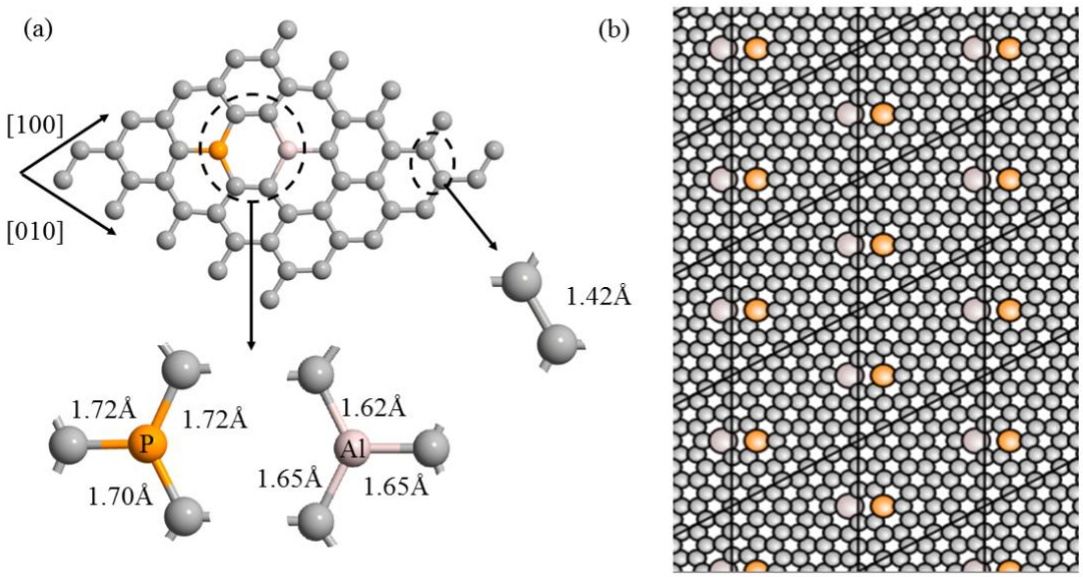


**Figure 4.1** Ground-state optimal structure of Al-P doped graphene, (a) Optimized bond lengths of Al—C, P—C and C—C (b) Extended structure of co-doped graphene considered for the energy band structure calculations [57].

**Table 4.1** Induced bandgap and C—dopant bond length in differently doped graphene

| **Material** | | **B-N doped graphene** | **Al-P doped graphene** | **Ga-As doped graphene** |
|---|---|---|---|---|
| Bandgap (eV) | | 0.24 | 0.24 | 0.55 |
| Bond length 1 (Å) | Acceptor | 1.47 | 1.62 | 1.71 |
| | Donor | 1.4 | 1.7 | 1.7 |
| Bond length 2 (Å) | Acceptor | 1.47 | 1.65 | 1.72 |
| | Donor | 1.41 | 1.72 | 1.72 |
| Bond length 3 (Å) | Acceptor | 1.48 | 1.65 | 1.72 |
| | Donor | 1.41 | 1.72 | 1.72 |

## 4.2 Transition Metal functionalization

### 4.2.1 Palladium decoration

In this method, Pd is used to functionalize the graphene surface. TMs have high adsorption capabilities as compared to other elements [87]. Mulliken population analysis shows that bond formation between C and Pd atom occurs due to interaction between $p_z$ orbital of C atom (which is perpendicular to the plane of C atoms) and d orbital of Pd valence band. After optimization, the bond length between the Pd and C is 5.44 Å as depicted in figure 9(a). The extended surface of Pd decorated graphene is shown in figure 9(b) with one Pd atom per $nm^2$.

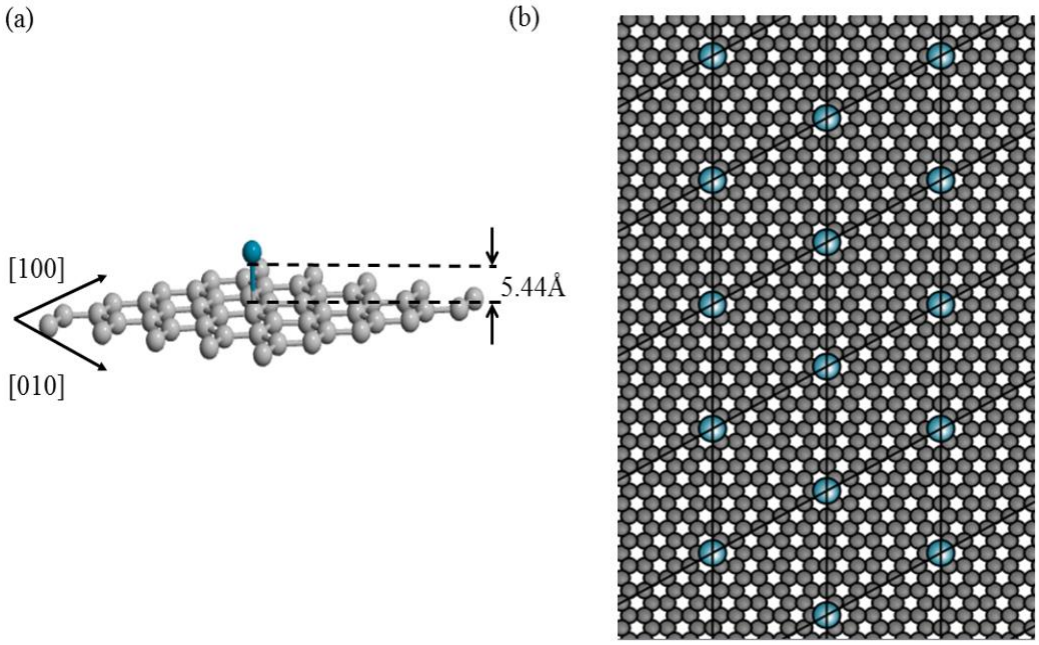


**Figure 4.2** (a) The Pd decorated graphene structure with C—Pd bond length (b) Extended surface of Pd decorated graphene considered for the energy band structure calculations[57].

### 4.2.2 Platinum decoration

Figure 10 illustrates the most stable position of Pt decorated graphene with periodic boundary conditions along (100) and (010) directions to resemble a semi-infinite sheet of graphene with one atom thickness along (001). In the lowest energy configuration obtained by the geometry optimization, Pt forms two covalent bonds with two nearest carbon atoms with a bond length of 2.1 Å. The bond population (signifies orbital overlapping) of 0.35 calculated by Mulliken analysis is interpreted as covalent bonding between the Pt and C atoms. Owing to the fact that

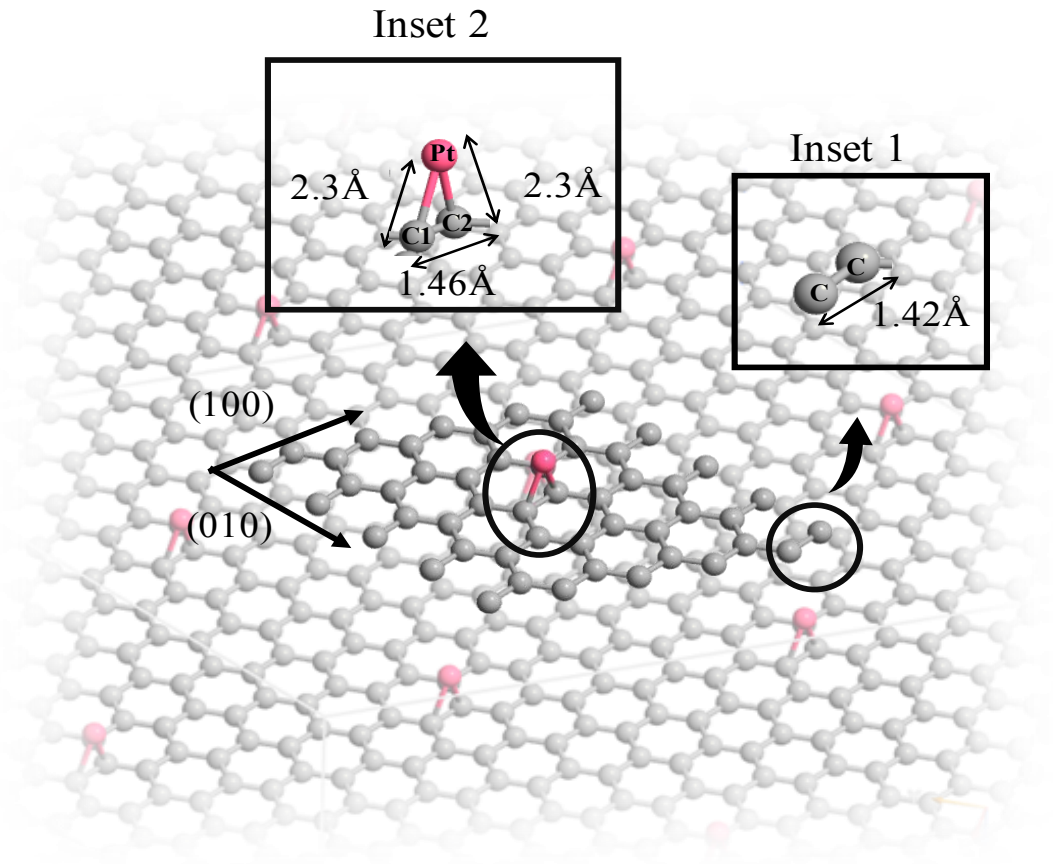


**Figure 4.3** C atoms in graphene are sp2 hybridized and bond to each other with 1.42 Å bond length (Inset 1). After decoration with Pt, the bond length between C1 and C2 increases to 1.46 Å (Inset 2), that affirms breaking of π bond [77].

both bondings have equal bond population value they show equal attraction towards Pt atoms.

To see the effect of Pt adsorption on the C—C bonding of carbon atoms (C1 and C2 as illustrated in inset 2 of figure 10) which are beneath the Pt atom, the bond length and bond population of the optimized C1—C2 is calculated. Adsorption of Pt atom on graphene increases C1—C2 bond length from 1.42 Å (Inset 1) to 1.46 Å (Inset 2) as shown in figure 10, which is due to the breaking of $\pi$ bonds and changing hybridization from $sp^2$ to $sp^3$ for these atoms. The same observation of weakening of C1—C2 bond length is also confirmed from the context of bond population, with the decoration of Pt, the bond population decreases from 0.9 to 0.7.

### 4.2.3 Increasing Concentration of Metal atoms

To get an intuitive perception of the interaction between the TM atoms on the graphene, two Pt atoms per supercell are considered and separated by 8.8 Å, 6.3 Å and 2.8 Å. After geometry optimization, the most stable structure of all three variants of two Pt decorated graphene (2Pt-graphene) is illustrated in figure 11. When Pt atoms are apart by 8.8 Å, null attraction occurs between the Pt atoms as zero Mulliken bond population exists between them. As the gap between the atoms decreases to 6.3 Å, weak intermolecular forces appeared between them as small orbital overlapping occurs which is affirmed through the Mulliken bond population of 0.1. For separation of 2.8 Å, a covalent bond is formed between Pt atoms with a Mulliken bond population of 0.28. This case gives the scenario in which the graphene is decorated with two covalently bonded Pt atoms structure per $nm^2$. Palladium also shows the same behaviour on increasing concentration.

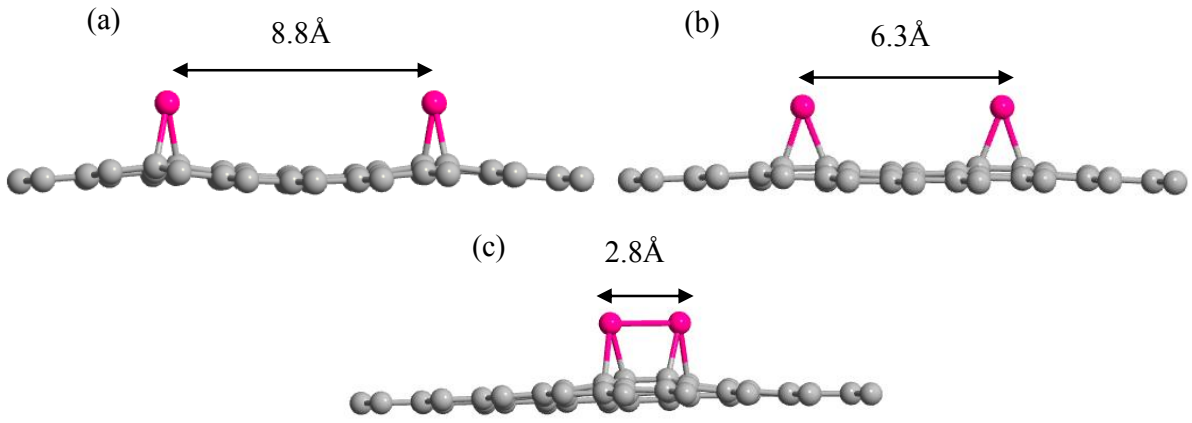


**Figure 4.4** Two Pt atoms decorated graphene where Pt atoms are separated by a distance of (a) 8.8 Å, with null attraction between Pt atoms, (b) 6.3 Å with weak intermolecular forces between Pt atoms, and (c) 2.8 Å with covalent bonding between Pt atoms [77].

## 4.3 Pristine/Defective graphene nanoribbon

As discussed in chapter 1, constraining the graphene in 1-dimension leads to the formation of the graphene nanoribbon (GNR) [33]. Under nonmagnetic conditions, Z-GNR is metallic [33]. However, A-GNR exhibit semiconducting properties. Therefore A-GNR is considered for this study. An investigation is carried on A-GNR with W=7 as shown in figure 12(a), as it belongs to the A-GNR family with the largest bandgap and provides efficient spatial distribution for molecule adsorption.

Crystalline solid exhibit three types of imperfections: point, line and planar defects. Out of these defect types, GNRs most commonly shows point defects such as vacancy defect and Stones Wales defect because it is a quasi-one-dimension material. As shown in figure 12, hydrogen is used for edge passivation of A-GNRs with a C—H bond length of 1.09Å. The structural details of the point defective A-GNR are discussed in the following paragraphs.

Similar to graphene, A-GNR is composed of hexagonally attached carbons (C) atoms. When one carbon atom is omitted from the hexagonal structure, a vacancy defect is induced in the A-GNR. Removing one atom from the geometry does not give the precise dimension of the defect. Therefore, the structure is relaxed energetically through geometry optimization. Figure 10(a) shows the optimized structure of A-GNR with vacancy defect along dimensionalities of deflected atoms due to the defect.

Figure 12(b) shows the structure of A-GNR with Stone Wales defect after geometry optimization. The Stone Wales defect occur during 90-degree rotation of the π bonded C atom lies on the shared edge of two hexagons and lead to the formation of two pentagons (P1 and P2 in figure 12(b)) and two heptagons (H1 and H2 in figure 12(b)) in the lattice[88]. As shown in the figure, the bond lengths of C1—C3, C2—C3, C5—C4 and C6—C4 increase from 1.42Å (undefective C-C bond length) to 1.5Å.

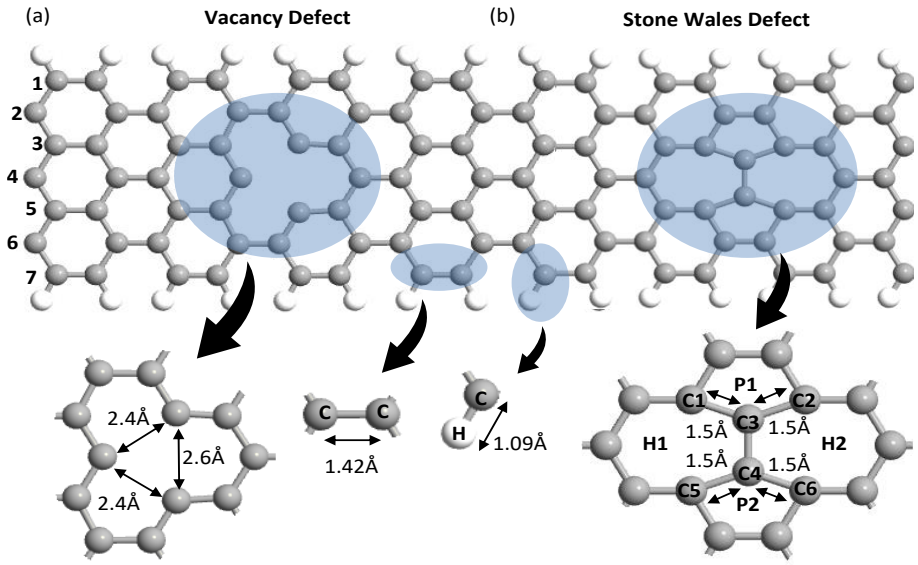


**Figure 4.5** The structural intricacies of (a) vacancy defective A-GNR and (b) Stones Wales defective A-GNR [87].

# Chapter 5. An Interaction Study with Biomarkers

In the interaction study, we only considered the cases in which the biomarker molecule made a strong interaction with the surfaced engineered graphene. As mentioned in chapter 1 two types of biomarker is considered, methanethiol, a biomarker for *helicobacter pylori* bacteria *(H. pylori)* and *porphyromonas gingivalis (P. Gingivalis) phylum* Bacteroidetes[57] and ethyl butyrate, a breath-born VOC biomarker for COVID-19 [62].

## 5.3 Methanethiol with compensated doped graphene

Characteristics of the interactions between the methanethiol[89] ($CH_3SH$) and graphene is determined by their binding energy ($E_{AD}$). Figures 13 present the optimized atomic structure of Al-P co-doped graphene in presence of a methanethiol molecule.

Compensated doped graphene shows a powerful association with the methanethiol through interaction between sulphur (S) and Al atoms. As it can be seen in the figure Al atom relocates itself by rising towards the methanethiol molecule causing distortion in the structure. However, there is no chemical bond formed between the biomarker and Al-P co-doped graphene and adsorption of biomarker by the graphene is due to physisorption phenomena.

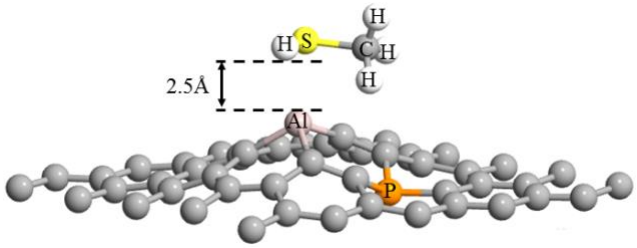


**Figure 5.1** Optimized structures of graphene-biomarker complex show Physiosorbed methanethiol biomolecule on Al-P doped graphene lattice [57].

Table 2 summarizes the calculated adsorption energies in proposed complexes. The values are counterpoise-corrected adsorption energies ($E_{AD+CP}$) (discussed in chapter 3) which correct the errors arising due to overlapping of basis orbitals of the two interacting atoms.

**Table 5.1** The total energies, adsorption energies between biomarker and graphene

| Material | $E_{AD+CP}$ (eV) |
|---|---|
| Methanethiol adsorbed Pd decorated graphene | -1.22 |
| Methanethiol adsorbed B-N doped graphene | -0.01 |
| Methanethiol adsorbed Al-P doped graphene | -0.90 |
| Methanethiol adsorbed Ga-As doped graphene | -0.02 |

The negative values of the $E_{AD+CP}$ in table 2 indicates the favourable host-guest molecules adsorption. Furthermore, larger negative $E_{AD+CP}$ corresponds to more efficient adsorption and consequently higher sensing functionalities toward methanethiol. Therefore, the comparison between the values shows that the graphene doped with B-N and Ga-As do not have efficient adsorption energy towards the indicated biomarker. As a result, for further analyzes, we have only considered Al-P doped graphene with the adsorption energies of -0.90 eV.

## 5.4 Biomarkers with transition metal decorated graphene

### 5.4.1 Methanethiol with Pd decorated graphene

Contrary to what was observed for the case of compensated graphene, figure 14 illustrates that a bond formation occurs between the methanethiol molecule and Pd-decorated graphene with adsorption energy -1.22 which is confirmed from the Mullikan bond population of 0.3. The involvement of the S atom in bond formation with Pd, confirms the occurrence of chemisorption representing stronger binding between the guest-host complex.

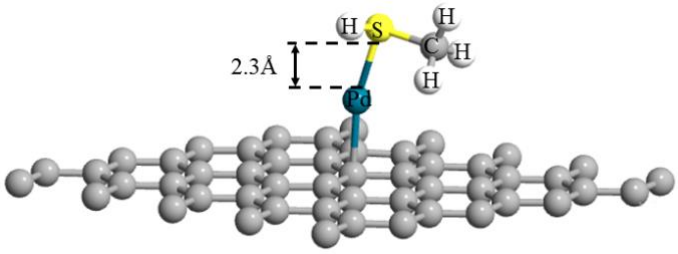


**Figure 5.2** Optimized structures of graphene-biomarker complex show Chemisorbed methanethiol biomolecule on Pd-decorated graphene lattice [57].

### 5.4.2 Ethyl Butyrate with Pt decorated graphene

Interaction between ethyl butyrate ($C_6H_{12}O_2$) and pristine graphene as well as surface engineered graphene is analyzed based on the counterpoise (CP) corrected adsorption energies [90]. (CP corrected adsorption energy eliminates the error that occurs due to basis set overlapping).

Upon studying interactions, it is found that ethyl butyrate is strongly adsorbed on Pt decorated graphene with an adsorption energy of -1.33 eV (this value is much higher than that of pristine graphene with the adsorption energy of -0.1 eV toward ethyl butyrate). Our calculations indicate that after optimization the main interaction is associated with the Oxygen atom (O2) of the

biomarker and Pt atom. Mulliken bond population of 0.23 confirms the covalent bond between O2 and Pt with a bond length of 2.1 Å as shown in figure 15. The formation of the covalent bond between host-guest material confirms the chemisorption. Moreover, it is observed that the adsorption creates slight deformation to the host molecule which is illustrated in figure 15 where translucent atoms show the structure of a free molecule and opaque atoms show the structure of an adsorbed molecule. Adsorption also slightly deforms the clar's structure of graphene around the Pt atom as shown in figure 15.

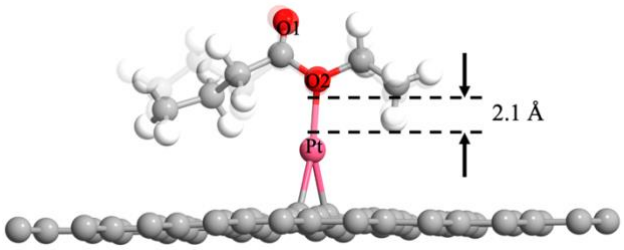


**Figure 5.3** Optimized structures of graphene-biomarker complex show Ethyl butyrate adsorbed Pt decorated graphene complex [77].

## 5.5 Methanethiol with vacancy defected A-GNR

Fig. 16 shows the optimized structure of the methanethiol adsorbed vacancy defective A-GNR complex. The most stable position of the biomarker is considered in terms of high adsorption energy. Adsorption of methanethiol of vacancy defected A-GNR exhibit adsorption energy of -2.1 eV. It is found that sulphur (S) acts as a bonding atom between the analyte and the host material. Due to the formation of vacancy, lone electrons exist in the C1, C2 and C3 atoms which shows strong enticement with the S atom of the analyte. Bond population which signifies the orbital overlapping factor of C1—S, C2—S and C3—S are 0.8, 0.8 and 0.7 with bond lengths 1.7

Å, 1.7 Å and 1.8 Å respectively, which confirms that the S atom of methanethiol made three covalent bonds with three C atoms of vacancy defective A-GNR.

Stone Wales defects do not show strong adsorption of methanethiol or ethyl Butyrate. Therefore it is not considered for interaction study.

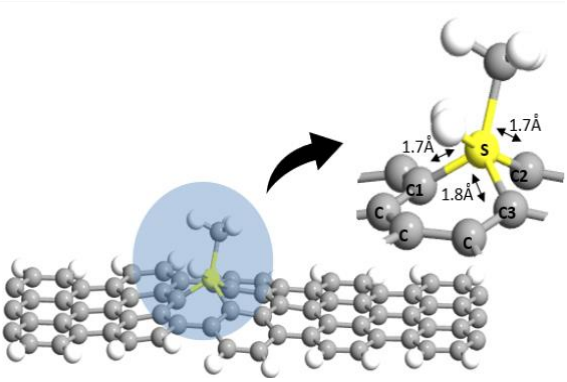


**Figure 5.4** The optimizes structure of Methanethiol adsorbed Vacancy defective A-GNR [87].

# Chapter 6. Electronic Properties

## 6.1 Al-P doped graphene before and after interactions with methanethiol

Figure 17 illustrates the calculated band structure of Al-P doped graphene before and after methanethiol adsorption. As it is seen, methanethiol adsorption increases the bandgap of the graphene from 0.24 eV to 0.45 eV. However, the intrinsic behaviour of the material remains the same after adsorption.

The effective density of states ($N_c$ or $N_v$) represents the sum of quantum states disseminated on the entire band in the form of two Dirac delta functions defined at the edge of the band[91]. $N_c$ ($N_v$) is a function of the carrier density of state mass ($m_e^{dos}$ or $m_h^{dos}$)[82]. $m_e^{dos}$($m_h^{dos}$) is the longitudinal (transverse ) effective mass and depends on the valley degeneracy of the energy bands [83]. In all cases, valley degeneracy is constant which means the values of longitudinal and transverse effective masses are affecting the $N_c$ and $N_v$. The longitudinal and transverse effective mass of electron decrease as conduction band minima (CBM) and valence band maxima (VBM) converge towards the Fermi level and they become massless at Dirac point which is the same as those of intrinsic graphene. After the adsorption of the biomarker, the bandgap increases, and consequently effective masses increase and as a result, $N_c$ and $N_v$ increase as tabulated in Table 3. Work function (Φ) expresses the total amount of energy required to knock out one electron from Fermi level to vacuum level [91] and it is inversely proportional to Fermi energy ($E_f$). Since adsorption of methanethiol decreases $E_f$, it leads to an

increment in the work function of methanethiol adsorbed complexes. As it is summarized in table 3, Al-P doped graphene has a work function of 4.2 eV which increases to 4.5 eV once the biomarker is adsorbed.

Boltzmann transport equation (BTE) with relaxation time approximation (RTA) explained in chapter 2 is used to calculate mobility (μ) in graphene structure. μ is directly proportional to the relaxation time of the carrier (Ʈ)[92]. Acoustic phonons scatterings have a major contribution to the value of Ʈ at room temperature. In graphene, there are three acoustic phonon modes, longitudinal acoustic (LA), transverse acoustic (TA) and out of plane acoustic (ZA) modes [93]. These modes affect the electron-phonon coupling matrix which is used to calculate Ʈ. As it is tabulated in table 3, our calculations show that carriers mobilities are decreased when methanethiol is adsorbed in Al-P doped graphene which affirms the velocity of the electrons and holes are also decreased. The structural distortion in Al-P graphene during the biomarker adsorption is the major cause of the reduction of mobility.

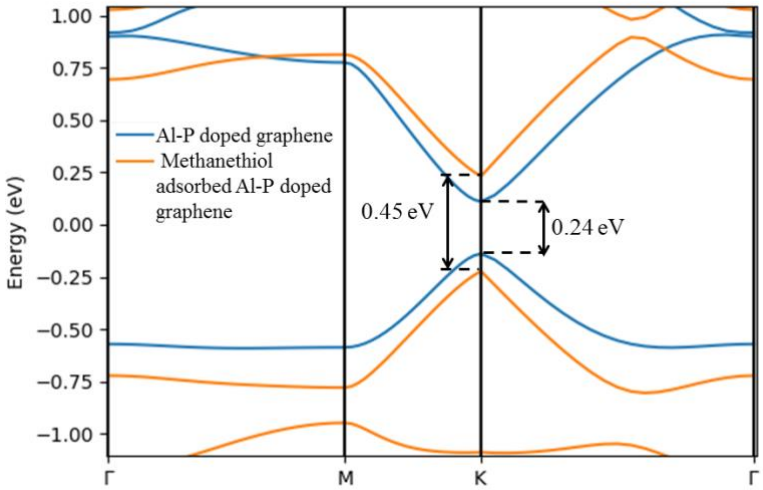


**Figure 6.1** Band structure and of Al-P doped graphene and methanethiol adsorbed Al-P doped graphene [77].

## 6.2 Pd decorated graphene before and after interactions with methanethiol

The Pd decorated graphene shows n-type behaviour with a bandgap of 0.018 eV. As is illustrated in figure 18 the adsorption of the biomarker increases the bandgap to 0.026 eV.

Our calculations show that the longitudinal and transverse effective mass of carriers increases as the methanethiol molecule is adsorbed on the graphene. Consequently, $N_c$ and $N_v$ also increase with adsorption. Biomarker adsorption also reduces the $E_F$ of the system as presented in table 3. Due to the inverse relationship of $E_F$ with $\Phi$, $\Phi$ of Pd-decorated graphene changes from 4.01 to 4.77 eV after adsorption.

Structural distortion increases the phonon scattering in the lattice which adversely affect the mobility of the material. Pd atom acts as a linking agent between graphene and analyte and impedes graphene from distortion. Therefore, adsorption of methanethiol increases mobility as summarized in table.3.

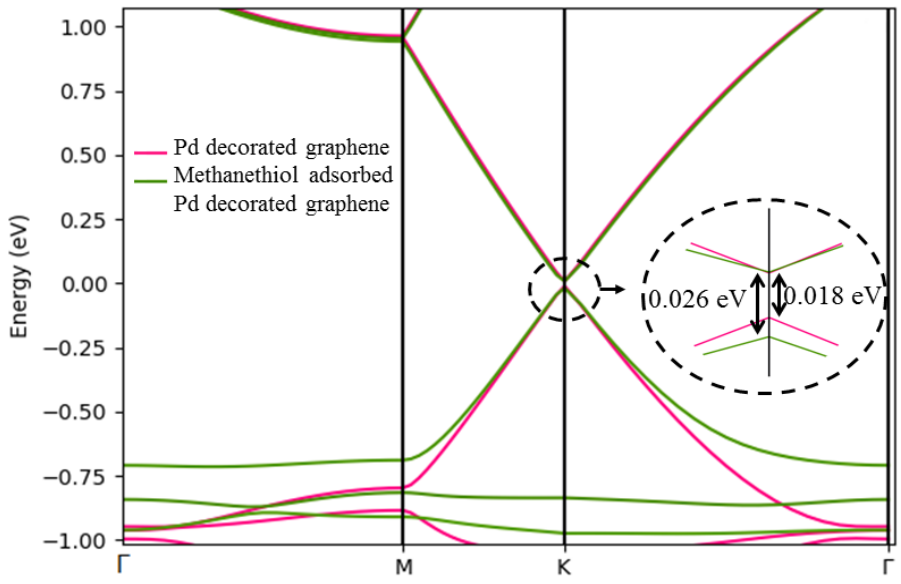


**Figure 6.2** Band structure and of Pd decorated graphene and methanethiol adsorbed Pd decorated graphene [77].

**Table 6.1** Physical parameters of different variants of graphene before and after methanethiol adsorption calculated by DFT analysis.

| | **Al-P doped graphene** | **Methanethiol adsorbed Al-P doped graphene** | **Pd decorated graphene** | **Methanethiol adsorbed Pd decorated graphene** |
|---|---|---|---|---|
| $\mathbf{E_g}$ **(eV)** | 0.24 | 0.45 | 0.018 | 0.026 |
| $\mathbf{E_{VBM} - E_F}$ **(eV)** | 0.12 | 0.23 | 0.011 | 0.019 |
| $\mathbf{E_{CBM} - E_F}$ **(eV)** | 0.12 | 0.23 | 0.007 | 0.007 |
| $\mathbf{E_F}$ **(eV)** | 5.32 | 4.99 | 4.97 | 4.88 |
| **Nature** | Semiconductor | Semiconductor | Semiconductor | Semiconductor |
| $\frac{m_{l(e)}}{\mathbf{m_e}}$ | 0.048 | 0.160 | 0.003 | 0.004 |
| $\frac{m_{t1(e)}}{\mathbf{m_e}}$ | 0.099 | 1.909 | 0.007 | 0.010 |
| $\frac{m_{t2(e)}}{\mathbf{m_e}}$ | 0.092 | 0.174 | 0.005 | 0.008 |
| $\frac{m_{l(h)}}{\mathbf{m_e}}$ | 0.052 | 0.164 | 0.003 | 0.004 |
| $\frac{m_{t1(h)}}{\mathbf{m_e}}$ | 0.108 | 2.287 | 0.007 | 0.010 |
| $\frac{m_{t2(h)}}{\mathbf{m_e}}$ | 0.098 | 0.176 | 0.005 | 0.008 |
| $\frac{\mathbf{m_e^{dos}}}{\mathbf{m_e}}$ | 0.120 | 0.596 | 0.00748 | 0.011 |
| $\frac{\mathbf{m_h^{dos}}}{\mathbf{m_e}}$ | 0.130 | 0.641 | 0.00748 | 0.011 |
| $\mathbf{N_c(cm^{-3})}$ | $1.04\times10^{18}$ | $1.15\times10^{19}$ | $1.61\times10^{16}$ | $2.88\times10^{16}$ |
| $\mathbf{N_v(cm^{-3})}$ | $1.17\times10^{18}$ | $1.28\times10^{19}$ | $1.61\times10^{16}$ | $2.88\times10^{16}$ |
| **Φ(eV)** | 4.200 | 4.500 | 4.010 | 4.700 |
| **χ (eV)** | 4.080 | 4.270 | 4.003 | 4.693 |
| $\mathbf{\mu_e\ (cm^2/Vs)}$ | $1.25\times10^{5}$ | $1.79\times10^{4}$ | $9.58\times10^{4}$ | $1.28\times10^{5}$ |
| $\mathbf{\mu_h(cm^2/Vs)}$ | $2.29\times10^{5}$ | $4.00\times10^{4}$ | $3.5\times10^{4}$ | $1.90\times10^{5}$ |

## 6.3 Pt decorated graphene before and after interactions with ethyl butyrate

DFT analysis results confirm that the decoration of Pt on the graphene opens the Dirac cones of the band structure of graphene and transforms it into a semiconductor with a bandgap of 0.15 eV as is illustrated in figure 19(a). As presented in table 4, VBM and CBM are equidistant from the Fermi level, which confirms the intrinsic nature of the hybrid structure. Adsorption of ethyl butyrate opens the bandgap to 0.16 eV as illustrated in figure 19(b) and made complex n-type in nature by making CBM closer to Fermi level ($E_{CBM} - E_F$) as tabulated in Table 4.

The density of states curve in figure 19(c) describes the number of the quantum states generated by the C and Pt atoms in surface engineered graphene. Decoration of Pt nullifies the states by 0.075 eV from the Fermi level and leads to the generation of a bandgap. Moreover, Pt augmented the number of quantum states at many energy levels as presented in figure 19(c). Adsorption of ethyl butyrate creates the permutation of quantum states which is affirmed through figure 19(d) where the density of states is illustrated for graphene with adsorbed ethyl butyrate.

In pristine graphene, VBM and CBM coincide with each other and consequently, the carrier masses are zero and there is no effective density of states ($N_c$ and $N_v$) at CBM and VBM. Hybrid with Pt open the bandgap, consequently, electrons have effective masses and form $N_c$ and $N_v$. Their values are given in table 4. Adsorption of the biomarker increases the bandgap which results in further increment in $N_c$ and $N_v$ which are also reported in table 4. Table 4 also provides data regarding the work function ($\Phi$) and electron affinity ($\chi$) of graphene under various conditions.

Mobility is highly dependent on the lattice structure. The crystal structure of Pt-decorated graphene is slightly deformed due to the interaction between the decorating material and base material. As adsorptions deform the clar's structures, carrier mobilities in graphene (as is shown

in Table 4) will be decreased when it is decorated by Pt atoms, and then decrease even further when the biomarker is adsorbed by its surface.

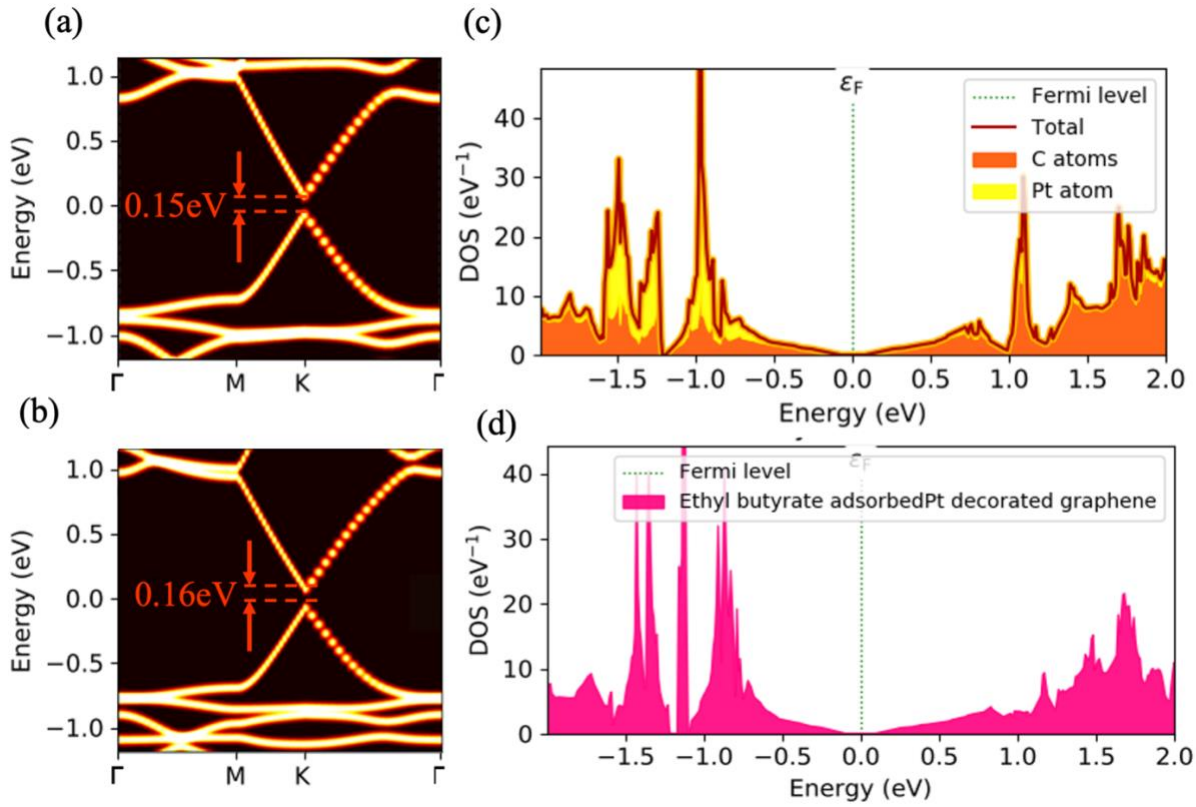


**Figure 6.3** Energy band structure of (a) the Pt decorated graphene, and (b) the ethyl butyrate adsorbed Pt decorated graphene. Density of states of (c) Pt decorated graphene, and (d) the Ethyl butyrate adsorbed Pt decorated [77].

### 6.3.1 Increasing concentration of Pt atoms per supercell

Decoration of Pt atoms results in potential fluctuation which leads to the formation or depletion of energy states in the forbidden or allowed energy ranges and this change in the allowed/ forbidden energy states results in increasing or decreasing of the bandgap [94]. In the 2Pt-graphene case, when Pt atoms are 8.8 Å apart, the bandgap increases to 0.158 eV as shown in figure 20(a). As Pt atoms come closer, at 6.3 Å separation gap, weak intermolecular forces exist

between Pt atoms as discussed in section 4.2.3 and the bandgap reduces to 0.04 eV as shown in figure 20(b). The parabolic dispersion relation is abrupted and irregularities are formed as localized states at CBM and VBM. Furthermore, it was observed that the bandgap of the graphene for the cases of 2.8 Å and 6.3 Å separations remains the same although in the case of 2.8 Å the material exhibits metallic behaviour as the Fermi level crosses the conduction band as shown in the inset of figure 20(c).

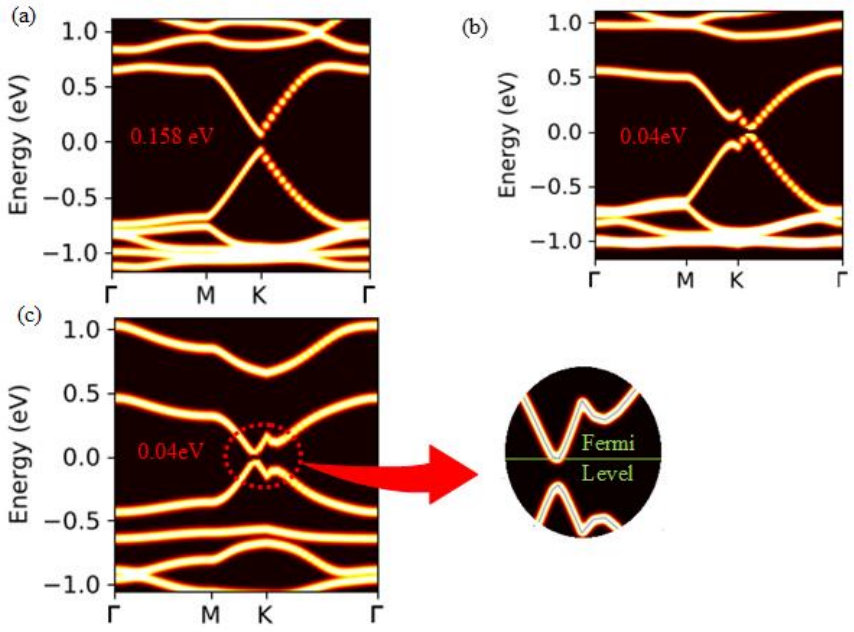


**Figure 6.4** Band structure of 2Pt-graphene where Pt atoms are separated by a distance of (a) 8.8 Å with bandgap 0.158 eV, (b) 6.3 Å with 0.04 eV bandgap, and (c) 2.8 Å showing metallic behaviour as the conduction band overlaps the Fermi level as shown in inset [77].

According to the results, as the Pt atoms are at a vicinity less than 8.8 Å, they start modulating the dispersion relation of the host material and create irregularities at the extrema of CBM and VBM. Therefore, to avoid the effects of interactions between the decorating atoms, in this study, we have only considered a graphene lattice decorated by two Pt atoms separated by 8.8 Å to

investigate the effect of biomarker concentrations on the sensing properties of the device. The optimized geometry of two ethyl butyrate molecules adsorbed on 2Pt-graphene shows that the bond formation is the same as the case of one ethyl butyrate adsorption on Pt decorated graphene as discussed in section 5.4.2.

To get a more authenticated view of the effect of biomarker concentration on the electronic structure of the graphene, two ethyl butyrate molecules are adsorbed on the 2Pt-graphene with a separation gap of 8.8 Å (only this separation gap allows the accommodation of two biomarker molecules and also parabolic relation remain undisturbed at this distance). Adsorption of two ethyl butyrate molecules on the 2Pt-graphene leads to a decrease in the bandgap of the host material to 0.13 eV. As summarized in table 4, after adsorption the Fermi level moves closer to CBM ($E_{CBM} - E_F$) which confirms its n-type semiconductor behaviour. The transition of intrinsic to slightly n-type behaviour after adsorption occurs due to electronic charge transfer from molecules to host material. Furthermore, as it is summarized in table 4, due to the change in the surface chemistry the effective density of states of 2Pt-graphene increases after the biomarker adsorption while the work function and electron affinity decrease.

Increasing the concentration of the adsorbate molecules affects the lattice by inducing the distortion in the periodic structure of the adsorbent material. These distortions increase the scattering events and consequently reduce the mobility of the material, as presented in table 4.

**Table 6.2** Physical parameters of different variants of Pt decorated graphene with Ethyl butyrate calculated by DFT analysis.

| **Properties** | **Pt decorated graphene** | **Ethyl butyrate adsorbed Pt decorated graphene** | **2 ethyl butyrate adsorbed 2 Pt decorated graphene** |
|---|---|---|---|
| $\mathbf{E_g}$ (eV) | 0.15 | 0.16 | 0.13 |
| $\mathbf{E_{VBM} - E_F}$ (eV) | 0.075 | 0.084 | 0.071 |
| $\mathbf{E_{CBM} - E_F}$ (eV) | 0.075 | 0.076 | 0.065 |
| Nature | Semiconductor | Semiconductor | Semiconductor |
| $\frac{\boldsymbol{m_{l(e)}}}{\mathbf{m_e}}$ | 0.026 | 0.027 | 0.052 |
| $\frac{\boldsymbol{m_{t1(e)}}}{\mathbf{m_e}}$ | 0.064 | 0.064 | 0.052 |
| $\frac{\boldsymbol{m_{t2(e)}}}{\mathbf{m_e}}$ | 0.181 | 0.192 | 2.78 |
| $\frac{\boldsymbol{m_{l(h)}}}{\mathbf{m_e}}$ | 0.026 | 0.027 | 0.055 |
| $\frac{\boldsymbol{m_{t1(h)}}}{\mathbf{m_e}}$ | 0.065 | 0.66 | 0.053 |
| $\frac{\boldsymbol{m_{t2(h)}}}{\mathbf{m_e}}$ | 0.186 | 0.205 | 5.04 |
| $\frac{\mathbf{m_e^{dos}}}{\mathbf{m_e}}$ | 0.105 | 0.109 | 0.315 |
| $\frac{\mathbf{m_h^{dos}}}{\mathbf{m_e}}$ | 0.106 | 0.113 | 0.384 |
| $\mathbf{N_c}$($cm^{-3}$) | $8.53\times10^{17}$ | $9.01\times10^{17}$ | $4.42\times10^{18}$ |
| $\mathbf{N_v}$($cm^{-3}$) | $8.65\times10^{17}$ | $9.51\times10^{17}$ | $5.95\times10^{18}$ |
| Φ(eV) | 4.02 | 3.96 | 3.64 |
| χ (eV) | 3.95 | 3.88 | 3.57 |
| $\boldsymbol{\mu_e}$ ($cm^2$/Vs) | $4.10\times10^5$ | $3.32\times10^5$ | $1.1\times10^5$ |
| $\boldsymbol{\mu_h}$($cm^2$/Vs) | $3.82\times10^5$ | $1.21\times10^5$ | $8.1\times10^4$ |

### 6.4 Vacancy defected A-GNR before and after interactions with methyl butyrate

The defect perturbs the periodicity of the crystal and fluctuates the potential of the material, which results in the formation of localised states in the forbidden energy area, known as defect induced trapping states. The two blue bands formed near the Fermi level (0) in fig 21(a) correspond to trapping states formed in the vacancy defective A-GNR. Due to the formation of the trapping states, the bandgap of A-GNR decreases from 1.47 eV to 0.15 eV, with the Fermi level stands at

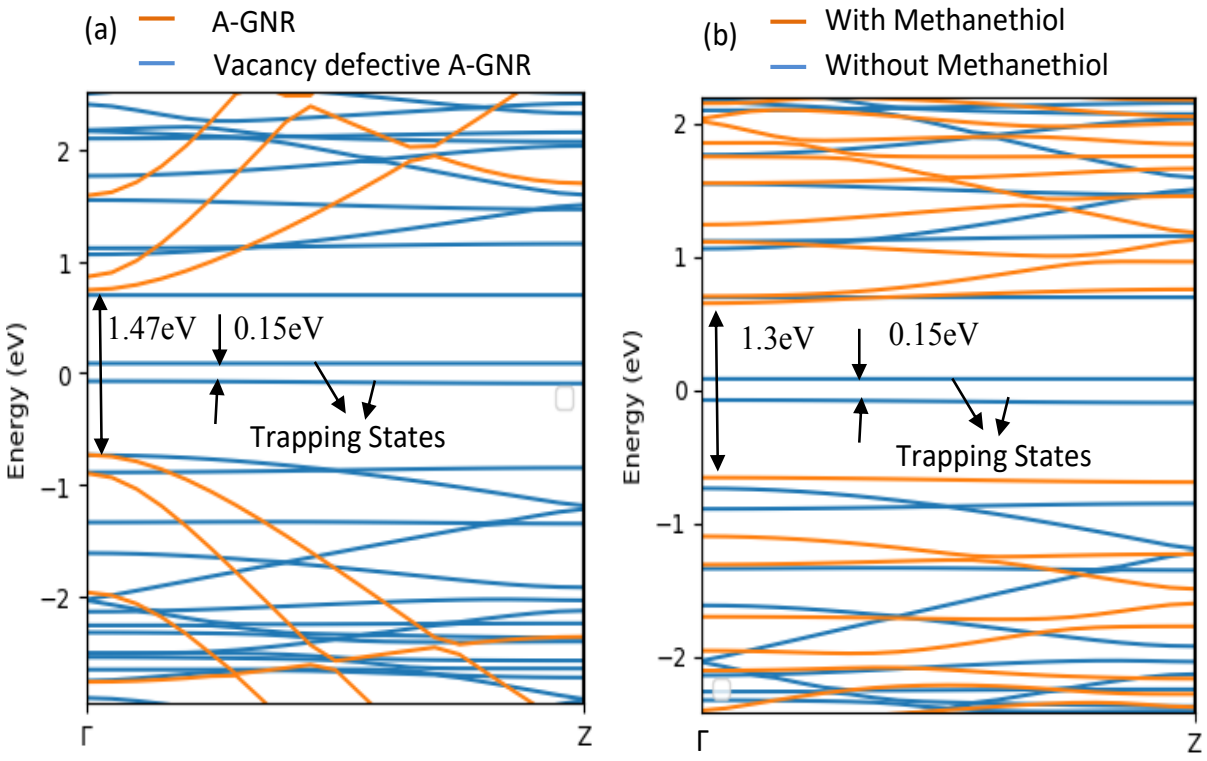


**Figure 6.5** Band structure comparison of (a) A-GNR with vacancy defective A-GNR (b) vacancy defective A-GNR with and without adsorption of methanethiol [87].

the middle of the bandgap, making A-GNR intrinsic. Methanethiol adsorption increases the material's bandgap from 0.15eV to 1.3eV, as shown in fig 21(b), by eliminating the trapping states formed near the Fermi level.

The parabolic base of CBM/VBM at Γ point of Brillouin zone is much broader in fig 21(a) for vacancy defective A-GNR than pristine A-GNR. Owing to effective mass relation with the CBM/VBM base, charge carriers of vacancy defective A-GNR are heavier than pristine A-GNR. Adsorption of methanethiol does not affect the masses of the charge carrier, and charge carriers remain the same as observed from the parabolic base of CBM/VBM of methanethiol adsorbed defective vacancy A-GNR with respect to the non-adsorbed host material.

Inducing the vacancy defect decreases the work function from 4.3 to 4.2 eV, but electron affinity increases from 3.56 to 4.12 as CBM level with respect to Fermi level decreases from 0.735 to 0.075 eV is shown in Table 4. The results show that the adsorption of biomarkers by the A-GNR decreases the work function and electron affinity of the material even further.

Significant variation in the electronic properties such as bandgap and work function of vacancy induced A-GNR is observed after the adsorption of the methanethiol with strong adsorption energy, which depicts strong binding of the biomarker with the proposed defective A-GNR and makes the vacancy induced defective A-GNR a promising material for biosensing of Methanethiol biomarker. The variations of bandgap and work function after the target molecule adsorption can be monitored as the sensing parameters.

**Table 6.3** Electronic properties of different variants of A-GNR

| | A-GNR | Vacancy defective A-GNR | Methanethiol adsorbed Vacancy defective A-GNR |
|---|---|---|---|
| **Bandgap (eV)** | 1.47 | 0.15 | 1.3 |
| **VBM (eV)** | 0.735 | 0.075 | 0.65 |
| **CBM (eV)** | 0.735 | 0.075 | 0.65 |
| **Work function (eV)** | 4.3 | 4.2 | 3.8 |
| **Electron affinity (eV)** | 3.56 | 4.12 | 3.15 |

# Chapter 7. Device Designing and Analysis

COMSOL Multiphysics is used to investigate the DC characteristics of the proposed GFET devices. The software efficiently allows assigning physical properties of materials to model the device. The investigated semiconducting properties of the functionalized graphene in the presence and absence of the biomarker (as summarized in Tables 3 and 4) are applied in the material properties section required by the model.

The Al-P doped GFET (AlP-GFET) and TM decorated GFET (Pd-GFET/Pt-GFET) performances are characterized by considering the effect of geometrical and physical parameters of the devices.

The impact of device parameters variation on the sensitivity of the sensor is discussed in the following sections.

A-GNR is 1D material. Therefore, drift-diffusion formalism no longer applies to devices modelled using A-GNR. Therefore, a Device study of A-GNR is not done in this work.

## 7.1 Device designing

A GFET is a three-electrode device, composed of a graphene channel between two electrodes and a gate contact to modulate the electronic response of the channel. The geometrical configuration of the proposed device is illustrated in figure 22. The device comprises a one atom thick graphene monolayer laying on a silicon-oxide/silicon ($SiO_2$/Si) substrate. The $SiO_2$ is an insulating layer, serving as a dielectric with a dielectric constant ($\varepsilon_r$) of 3.99. For the sake of calculations, the boundary conditions at all terminals are considered ohmic.

I-V measurements are used to determine the performance and characteristics of the device. These measurements are subjected to varying the dimensions of the graphene channel, and it's surface chemistry (functionalization), the thickness of the dielectric layer, and the doping concentration of the Si substrate.

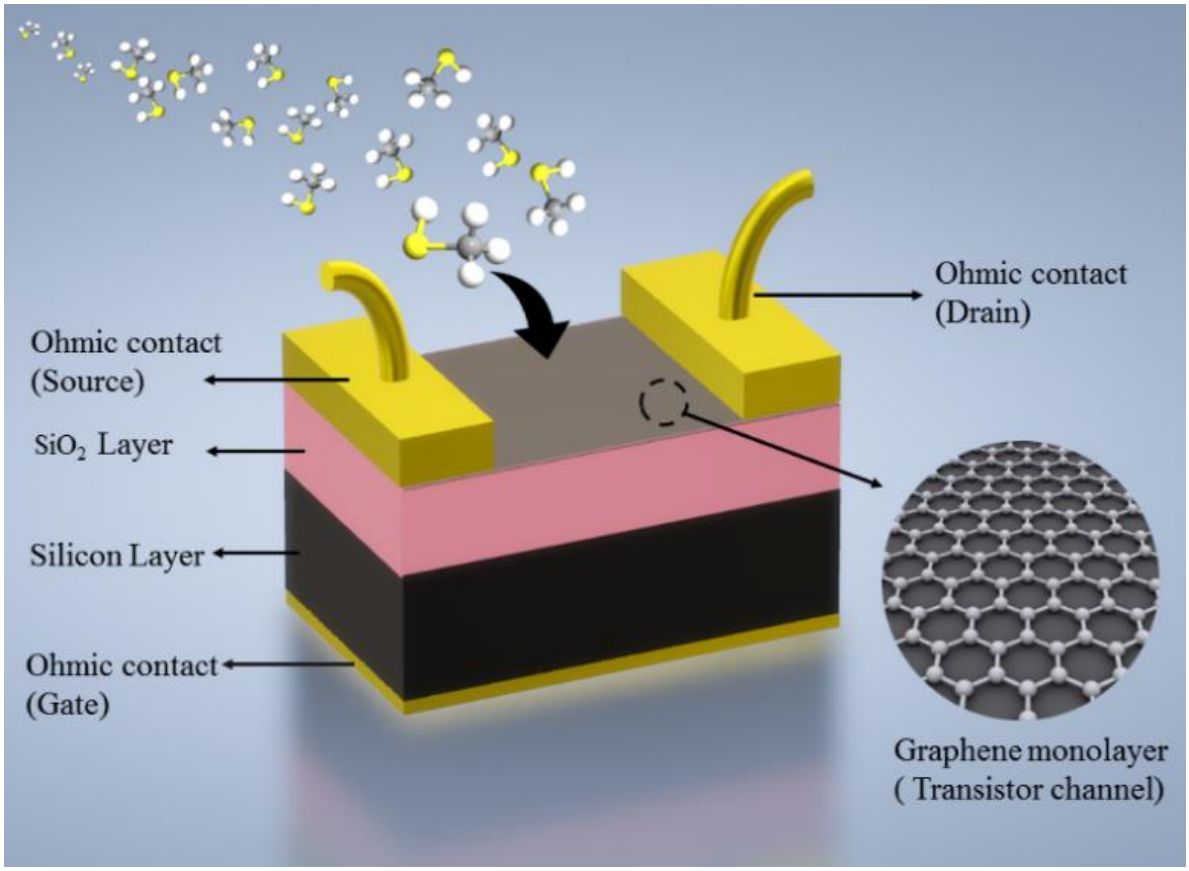


**Figure 7.1** The proposed GFET model. The proposed GFET model. The back-gate structure enables binding of the biomarker to the channel surface [57].

The graphene layer serves as a channel in the above structure and must be semiconducting. As it is a semimetal material in nature, we manipulate its band structure to transfer it to a semiconductor using several methods to induce bandgap in the graphene band structure discussed in chapter 4

## 7.2 DC characteristics of the device

In this section, the electrical characteristics of the AlP-GFET and Pd-GFET devices in the absence of biomarkers are evaluated. Pt-GFET shows the same trends as Pd-GFET. Therefore, its characteristics are not discussed separately.

For these analyzes, the channel length (L, the source-drain spacing) and channel width (W) of the device are considered 2 μm and 1 μm respectively. A p-type Si with a doping concentration of $10^{18}$ $cm^{-3}$ is used as the substrate. While the source is grounded the drain current ($I_d$) is measured by sweeping the gate voltage ($V_g$) from 0 to 2 V at a drain voltage ($V_d$) of 10 mV. I-V characteristics of the devices are shown in figure 23(a) (AlP-GFET) and (b) (Pd-GFET). As it is shown two distinct regions appear in the graphs, negative differential resistance (NDR) and positive differential resistance (PDR). A minimum happens as these two regions meet which is known as Dirac point at gate voltage, $V_n$ (neutral voltage). According to the graphs, the $V_n$ of

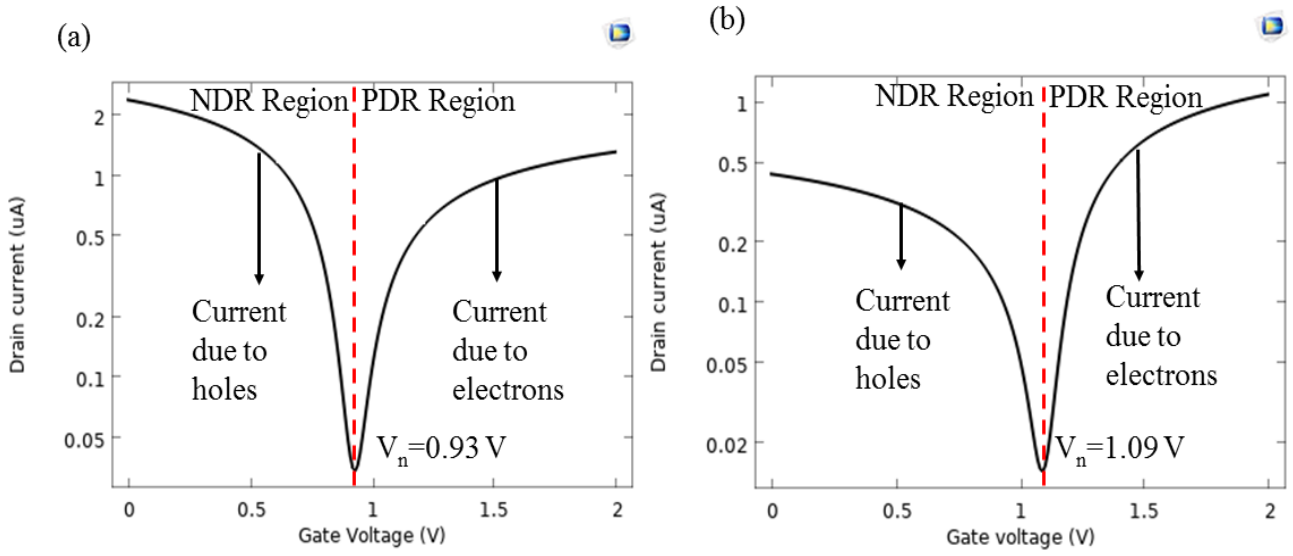


**Figure 7.2** I-V characteristics show two distinct regions and the particular Vn for a) AlP-GFET, b) Pd-GFET [57].

0.93 V and 1.09 V were observed for AlP-GFET and Pd-GFET, respectively. $V_n$ for Pt-GFET is 1.073V.

This peculiar behaviour of the I-V characteristics of the device is due to the ambipolar transport nature of graphene which implies the coupled motion of holes and electrons. Therefore, the charge carrier concentration along the graphene channel gives more insight into the $I_d$-$V_g$ curve discussed in figure 23.

The density of the carriers for AlP-GFET and Pd-GFET devices versus the gate voltage are shown in figures 24(a) and 24(b) respectively. The figures show that the holes are the majority carrier when the value of $V_g$ is below the value of $V_n$ of the device. At $V_n$ the concentration of both carriers is equal and as $V_g$ increases beyond $V_n$ a channel inversion is observed and the electrons will dominate the carrier concentrations.

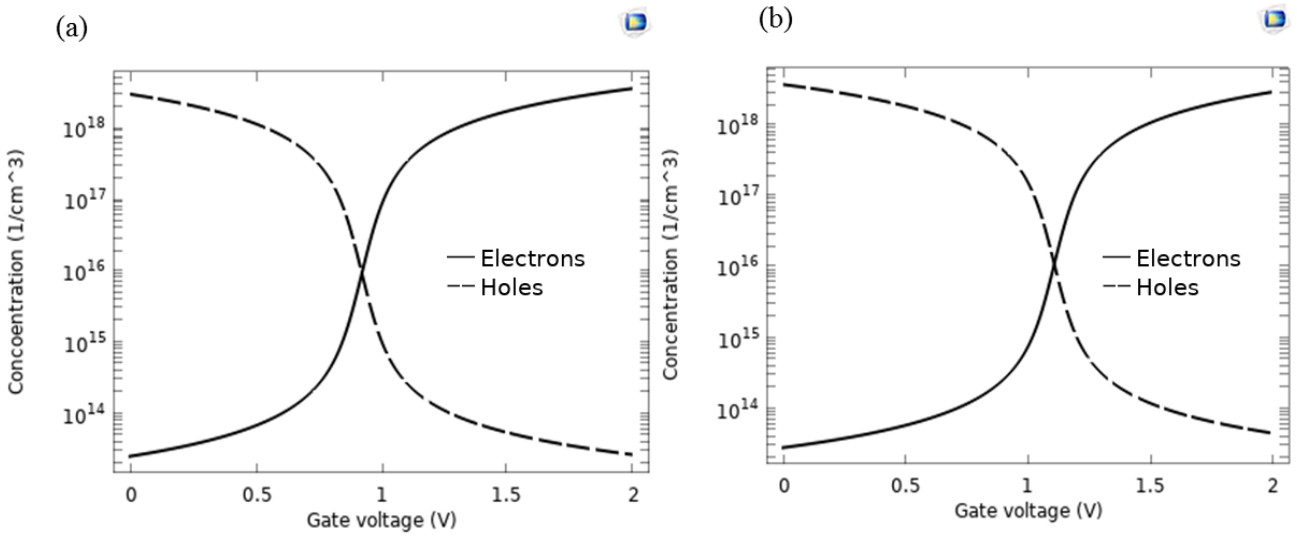


**Figure 7.3** Carrier concentration in the graphene channel versus Vg for a) AlP-GFET, b) Pd-GFET. It confirms the occurrence of inversion of the device channel at Vn [57].

The conductance of the channel is determined by the abundance of charge carriers which is influenced by the applied gate voltage. The conductance, in return, determines the $I_d$. Therefore, in figure 23, the negative slope of $I_d$ in the NDR region corresponds to the decreasing trend of

carrier hole concentration and the positive slope of $I_d$ in the PDR region corresponds to the increasing trend of the carrier electron concentration.

Figure 25(a) illustrates the $I_d$-$V_g$ curve of AlP-GFET at different drain voltages. It is observed that with an increment of the drain voltage, the I-V curve shift toward the higher current values. $V_n$ of 0.93 V, remains nearly constant for all $V_d$ values. $I_d$-$V_g$ characteristics of Pd-GFET shown in figure 25(b) follows the same trend as discussed for AlP-GFET. For this device, $V_n$ occurs at the voltage of 1.09 V which is higher than what was observed for AlP-GFET. Moreover, the lower current intensity of Pd-GFET is due to the lower carrier mobilities in this device compared to AlP-GFET as summarized in table 3.

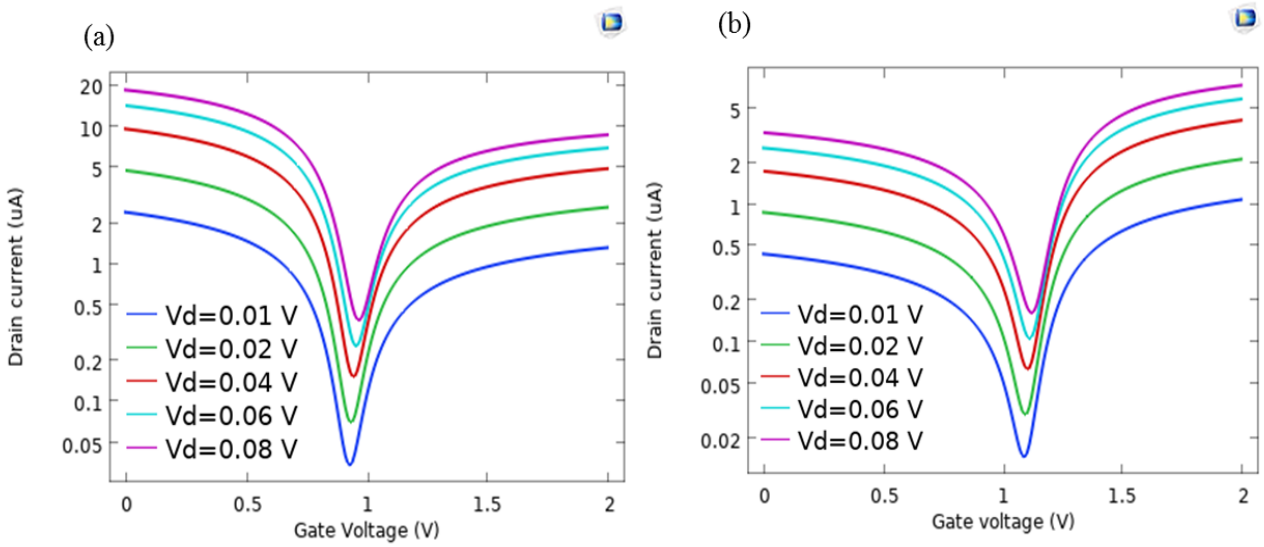


**Figure 7.4** I-V characteristics as a function of applied Vd for a) Al-P doped GFET b) Pd-decorated GFET. According to the graphs Vn of the devices remains constant as Vd varies [57].

To give a more authenticated perception of the device study, $I_d$-$V_g$ curves are calculated at $V_d$ of 10 mV for the devices with different channel dimensions (W×L). Figures 26(a) and 26(b) present the obtained results for the AlP-GFET and Pd-GFET devices respectively. As the results show,

the value of $V_n$ for both devices remain constant, and it is independent of the device geometry. This is one of the positive characteristics of the device that shows the sensing properties of the device will not be affected by the structural device dimensions. However, the device $I_d$ is a function of channel length and width, $I_d \propto \frac{W}{L}$ .The effect of the channel dimension on the device $I_d$ follows the following equation[95]

$$I_d = \frac{W}{L} \int_{V_s}^{V_d} (q\mu_p p + q\mu_n n + q\frac{\mu_p+\mu_n}{2} n_{pud}) dV \tag{7.1}$$

where the parameters $W$and $L$ are width and length of the channel respectively, $\mu_n$and $\mu_p$ are electron and hole mobility respectively and $\sigma = q\mu_n n + q\mu_p p$ is the conductivity of the channel. The term, $q\frac{\mu_p+\mu_n}{2} n_{pud}$ denotes the residual charge occurs due to the spatial homogeneity.

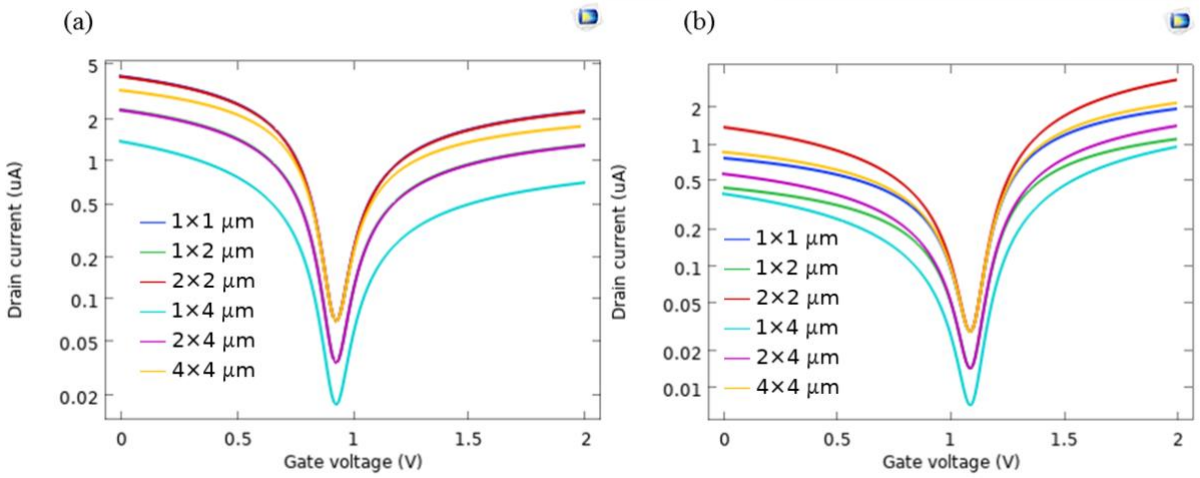


**Figure 7.5** I-V characteristics as a function of applied Vd for a) Al-P doped GFET b) Pd-decorated GFET. According to the graphs Vn of the devices remains constant as Vd varies [57].

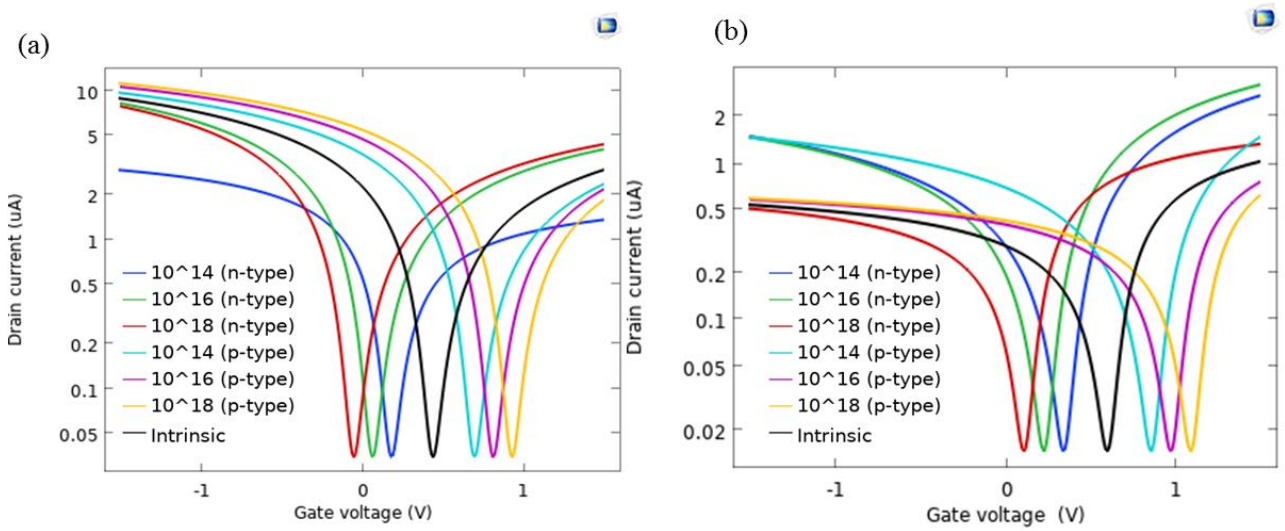


**Figure 7.7** I-V characteristics as a function of doping type and concentration for a) AlP-GFET b) Pd-GFET[57].

We have also investigated the characteristics of the device with respect to the electrical properties of the silicon substrate for both variants of the device. The results show that they have a significant effect on the value of $V_n$ as we change the doping type and its concentration of the substrate. The I-V characteristics in figures 27(a) (AlP-GFET) and 27(b) (Pd-GFET) illustrate

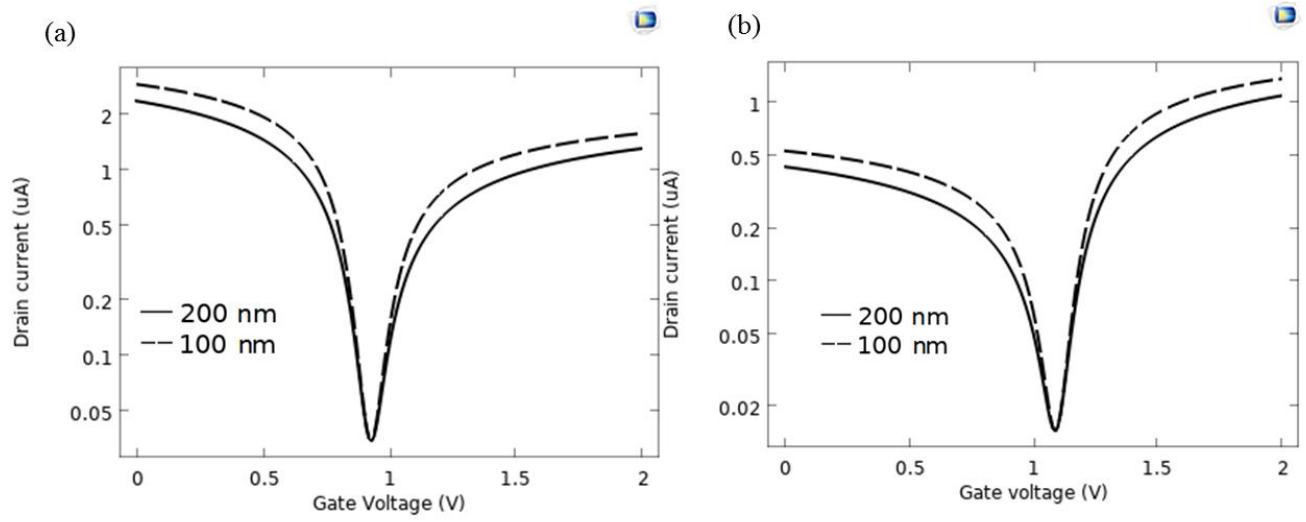


**Figure 7.6** I-V characteristics as a function of dielectric layer thickness a) AlP-GFET b) Pd- GFET [57]

that by increasing the concentration of dopants the position of $V_n$ moves toward higher voltages for p-type substrates while it moves toward lower voltages for the n-type substrate case.

Figures 28(a) and 28(b) show the measured $I_d$-$V_g$ for AlP-GFET and Pd-GFET devices respectively for two different oxide thicknesses of 200 nm and 400 nm. According to the graphs that the variation of the oxide layer thickness does not affect the sensing properties of the devices as the value of $V_n$ remains the same for both cases.

## 7.3 Detection of methanethiol biomarker

To check the sensitivity of the device against biomarkers, typically the device DC characteristics are evaluated in presence of a biomarker and compared with a reference test in the absence of biomarkers.

For this study, a device with channel dimensions of 1 x 2 $\mu m^2$ (W×L) and a p-type substrate with doping concentration $10^{18}$ $cm^{-3}$ is considered. $V_g$ is swept from 0 to 2 V while a constant $V_d$ of 10 mV is applied on the drain. One biomolecule per $nm^2$ was considered for the adsorption concentration of the biomarker on the graphene layer.

Figures 29(a) and 29(b) illustrate the $I_d$-$V_g$ characteristics of the AlP-GFET and Pd-GFET respectively in presence of the methanethiol as compared to a reference test in absence of the biomarker.

$I_d$-$V_g$ curves obtained for AlP-GFET show a clear shift in $V_n$ from 0.93 V to 0.63 V after the adsorption of methanethiol by the channel surface, while for the Pd-GFET was changed from 1.09 V to 0.42 V. The shift in $V_n$ is attributed to the change of $\mu$, bandgap, $N_c$ or $N_v$ and $\Phi$ of the functionalized graphene once it is exposed to the methanethiol molecule. As summarized in table 3, these physical quantities show variation after adsorption of methanethiol, which affects the $V_n$

value. The observed shift in $V_n$ for the Pd-GFET is larger than that of the AlP-GFET which affirms the higher sensitivity to the biomarker for this device.

It is observed that the overall current intensity for AlP-GFET decreases after the adsorption of the biomarker. However, in the case of Pd-GFET, the intensity of the current slightly increases after biomarker adsorption. This behaviour of the device corresponds to the effect of adsorption on the carrier mobility of the graphene channel (as summarized in table 3). The increase in mobility of the carriers will be correlated with an increase in the $I_d$ of the device and vice versa.

Based on the results discussed, Vn of the device is only a function of semiconductive properties of the graphene channel and varies by functionalization of the graphene and its interaction with the molecules. The geometry of the device and the biasing parameters does not alter the $V_n$ and therefore the sensitivity of the sensors towards exposure to methanethiol could be simply defined as $S \cong \left|\frac{\Delta Vn}{Vn}\right|$. The calculated sensitivity of the AlP-GFET towards methanethiol when the $V_n$ changes from 0.93 V to 0.63 V is 32.25%, similarly $V_n$ in the Pd-GFET changes from 1.09 V to 0.42 V which shows 60.55% sensitivity towards this biomarker.

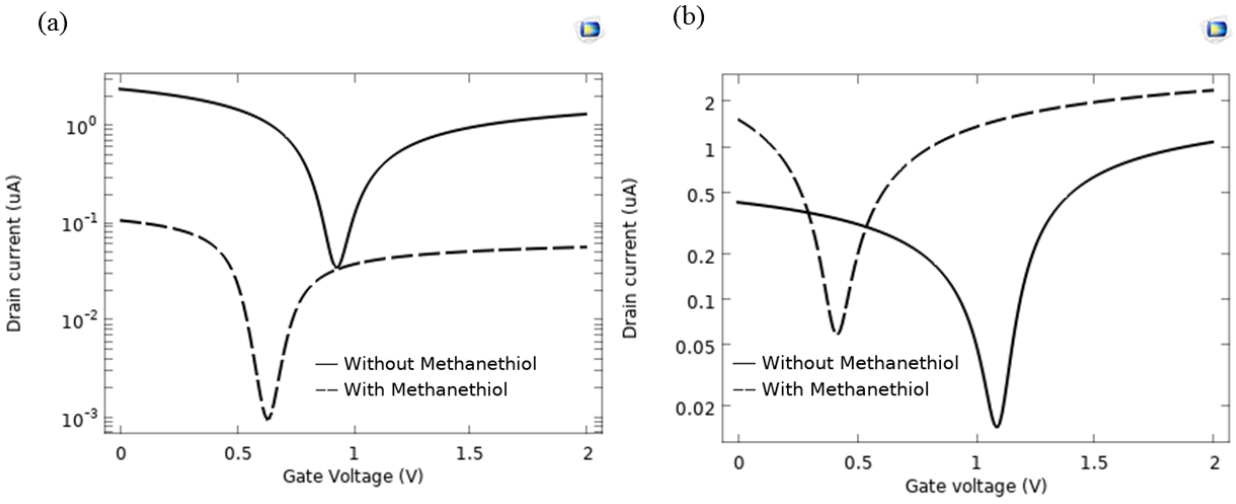


**Figure 7.8** I-V characteristics before and after adsorption of methanethiol for a) AlP-GFET, b) Pd-GFET [57].

## 7.4 Detection of ethyl butyrate biomarker

The exposure of the Pt-decorated graphene layer to ethyl butyrate changes the physical properties of the Pt-GFET channel (as summarized in chapter 5) which shifts the $V_n$ of the sensor device. Therefore, the I-V characteristics of the device before and after the attachment to the biomarker are studied. The simulated results are carried on one molecule of biomarker per $nm^2$ ($\sim 10^6$ molecules).

As it is illustrated in figure 30(a) the adsorption of the biomarker on the device channel changes the $V_n$ of the Pt-GFET from 1.07 V to 1.23 V. The intensity of the drain current is decreased, and the device is exposed to the biomarker although the charged carrier concentration remained in the same range as shown on figure 30(b). This can be explained by the decrements in the carrier

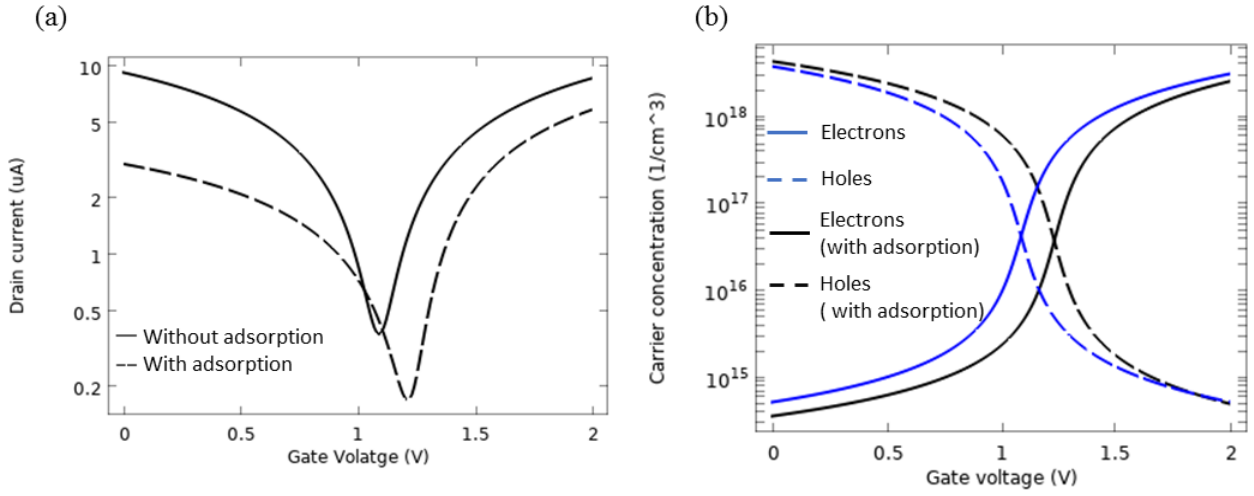


**Figure 7.9** (a) Sensing characteristics of Pt-GFET (b) carrier concentration of electron and holes of ethyl butyrate adsorbed Pt-GFET [77].

mobility of Pt decorated graphene from the adsorption as summarized in table 4. The sensitivity for this device is 9.4%.

### 7.5 Effect of concentration

Figure 31 shows the I-V characteristics of the designed sensors at a constant drain voltage. It is vivid from the figure that, increasing the concentration of the biomarker shifts the $V_n$ towards higher values of the $V_g$. As discussed above, the increment in the concentration of the biomarker decreases the work function/electron affinity of the material, which affects the work function difference between the substrate material and channel that leads to the modulation of Dirac point and consequently $V_n$. Moreover, increasing the concentration of biomarkers decreases the current intensity of the material which occurs due to the reduction of the mobility of the carries after adsorption.

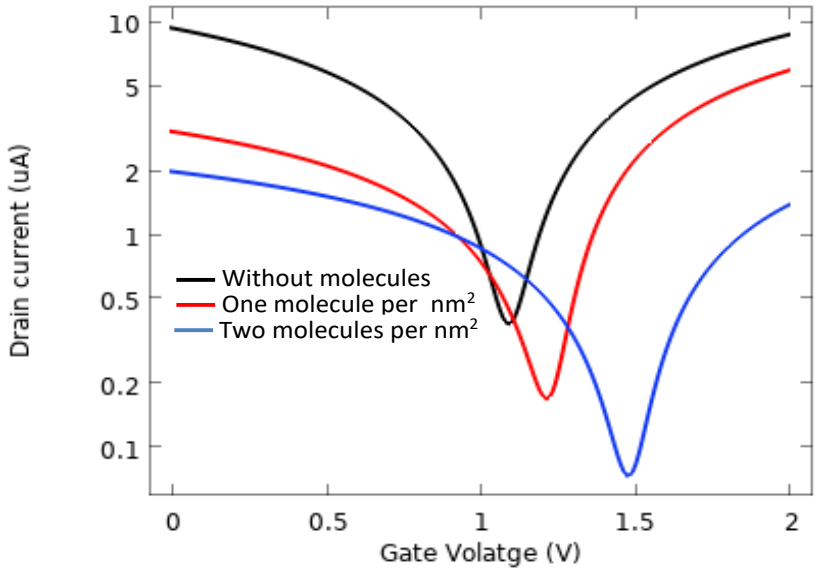


**Figure 7.10** Sensing characteristics of Pt decorated GFET at various concentrations of ethyl butyrate biomarker [77].

# Chapter 8. Conclusion and Future Scope

## 8.1 Conclusion

In this work, we demonstrated the possibility of using GFET biosensor for the detection of methanethiol biomarker which used to identify diseases caused by microorganisms such as *helicobacter pylori* bacteria (*H. pylori*) and *porphyromonas gingivalis* (*P. Gingivalis*) phylum Bacteroidetes and ethyl butyrate biomarker for COVID-19. The surface of the graphene layers is manipulated using three methods a) doping the graphene crystals and b) decorating the surface of the graphene with TMs c) graphene nanoribbons before using it as the channel of the GFET.

DFT analysis is also used to analyze the semiconductor properties such as bandgap, the effective mass of the charge carriers, mobility of the carriers and density of states of the bandgap engineered graphene and its complex with and without adsorption of methanethiol.

The device was designed and characterized using COMSOL Multiphysics. The NDR characteristic of the graphene which is due to its ambipolar behaviour was observed using 3-terminal measurements. The deep appeared in the I-V characteristics of the device is used to study the sensitivity of the sensors. The results show that the device characteristic is only sensitive to the doping level of the silicon substrate otherwise is independents of other physical parameters of the device. However, our investigations show that electrical properties of the functionalized graphene layers particularly in the absence and presence of the biomarkers are largely affected the characteristics of the sensor. The device is more sensitive to the adsorbed biomarkers in the case of TM based GFETs.

## 8.2 Future scope

To improve this research work, the following investigation can be performed:

- Simulation is done in this research work. Further, experimental research can be carried to fabricate this biosensor device.
- Adsorption can be performed in the presence of electric field to analyze the effect of electric field on adsorption. For this type of analysis via DFT, the first geometry optimization should be performed on graphene with electric field and then desired analyte molecule adsorbed on the surface graphene via second geometry optimization with electric field.
- Graphene Nanoribbon based device modelling can be performed using the non-equilibrium green's function formalism. This type of formalism is used to design nanoscale devices. This can lead to designing a single-molecule detector nanodevice whose channel width is only capable of adsorbing one molecule of the target analyte.
- Determining the appropriate surface engineering technique to detect various types of biomarkers.

# References


[1] S. Talebian, G. G. Wallace, A. Schroeder, F. Stellacci, and J. Conde, "Nanotechnology-based disinfectants and sensors for SARS-CoV-2," *Nat. Nanotechnol.*, vol. 15, no. 8, pp. 618–621, 2020, doi: 10.1038/s41565-020-0751-0.

[2] X. Gan, H. Zhao, R. Schirhagl, and X. Quan, "Two-dimensional nanomaterial based sensors for heavy metal ions," *Microchimica Acta*, vol. 185, no. 10. Springer-Verlag Wien, pp. 1–30, Oct. 01, 2018, doi: 10.1007/s00604-018-3005-1.

[3] C. Zhu, D. Du, and Y. Lin, "Graphene-like 2D nanomaterial-based biointerfaces for biosensing applications," *Biosensors and Bioelectronics*, vol. 89. Elsevier Ltd, pp. 43–55, Mar. 15, 2017, doi: 10.1016/j.bios.2016.06.045.

[4] S. Mao *et al.*, "Two-dimensional nanomaterial-based field-effect transistors for chemical and biological sensing," *Chemical Society Reviews*, vol. 46, no. 22. Royal Society of Chemistry, pp. 6872–6904, Nov. 21, 2017, doi: 10.1039/c6cs00827e.

[5] A. Molle, J. Goldberger, M. Houssa, Y. Xu, S. C. Zhang, and D. Akinwande, "Buckled two-dimensional Xene sheets," *Nature Materials*, vol. 16, no. 2. Nature Publishing Group, pp. 163–169, Feb. 01, 2017, doi: 10.1038/nmat4802.

[6] P. Singh, D. K. K. Randhawa, Tarun, B. C. Choudhary, G. K. Walia, and N. Kaur, "First principles investigation on armchair zinc oxide nanoribbons as uric acid sensors," *J. Mol. Model.*, vol. 26, no. 1, Jan. 2020, doi: 10.1007/s00894-019-4243-9.

[7] T. Tarun, D. K. K. Randhawa, P. Singh, B. C. Choudhary, G. K. Walia, and N. Kaur, "Analysis of uric acid adsorption on armchair silicene nanoribbons: a DFT study," *J. Mol. Model.*, vol. 26, no. 3, Mar. 2020, doi: 10.1007/s00894-020-4313-z.

[8] T. Tarun, P. Singh, H. Kaur, G. K. Walia, D. K. K. Randhawa, and B. C. Choudhary,

"Defective GaAs nanoribbon–based biosensor for lung cancer biomarkers: a DFT study," *J. Mol. Model. 2021 279*, vol. 27, no. 9, pp. 1–13, Aug. 2021, doi: 10.1007/S00894-021-04889-9.

[9] L. J. Carter *et al.*, "Assay Techniques and Test Development for COVID-19 Diagnosis," *ACS Cent. Sci.*, vol. 6, no. 5, pp. 591–605, May 2020, doi: 10.1021/acscentsci.0c00501.

[10] A. Bolotsky *et al.*, "Two-Dimensional Materials in Biosensing and Healthcare: From in Vitro Diagnostics to Optogenetics and beyond," *ACS Nano*, vol. 13, no. 9, pp. 9781–9810, May 2019, doi: 10.1021/acsnano.9b03632.

[11] R. Vargas-Bernal, "Graphene against Other Two-Dimensional Materials: A Comparative Study on the Basis of Electronic Applications," in *Two-dimensional Materials - Synthesis, Characterization and Potential Applications*, InTech, 2016.

[12] E. W. Hill, A. Vijayaragahvan, and K. Novoselov, "Graphene sensors," *IEEE Sens. J.*, vol. 11, no. 12, pp. 3161–3170, 2011, doi: 10.1109/JSEN.2011.2167608.

[13] A. N. Grigorenko, M. Polini, and K. S. Novoselov, "Graphene plasmonics," *Nat. Photonics*, vol. 6, no. 11, pp. 749–758, 2012, doi: 10.1038/nphoton.2012.262.

[14] K. Nomura and A. H. MacDonald, "Quantum transport of massless dirac fermions," *Phys. Rev. Lett.*, vol. 98, no. 7, pp. 1–4, 2007, doi: 10.1103/PhysRevLett.98.076602.

[15] Y. Kanai *et al.*, "Graphene Field Effect Transistor-Based Immunosensor for Ultrasensitive Noncompetitive Detection of Small Antigens," *ACS Sensors*, vol. 5, no. 1, pp. 24–28, 2020, doi: 10.1021/acssensors.9b02137.

[16] A. Salehi-Khojin *et al.*, "Graphene Sensors: Polycrystalline Graphene Ribbons as Chemiresistors (Adv. Mater. 1/2012)," *Adv. Mater.*, vol. 24, no. 1, pp. 52–52, 2012, doi: 10.1002/adma.201190200.

[17] A. Soltani *et al.*, "Direct nanoscopic observation of plasma waves in the channel of a graphene field-effect transistor," *Light Sci. Appl.*, vol. 9, no. 1, 2020, doi: 10.1038/s41377-020-0321-0.

[18] M. Salehirozveh, P. Dehghani, M. Zimmermann, V. A. L. Roy, and H. Heidari, "Graphene Field Effect Transistor Biosensors based on Aptamer for Amyloid-β Detection," *IEEE Sens. J.*, vol. 20, no. 21, pp. 1–1, 2020, doi: 10.1109/jsen.2020.3000583.

[19] I. Fakih *et al.*, "Selective ion sensing with high resolution large area graphene field effect transistor arrays," *Nat. Commun.*, vol. 11, no. 1, pp. 1–12, 2020, doi: 10.1038/s41467-020-16979-y.

[20] F. De Nicola *et al.*, "Graphene Plasmonic Fractal Metamaterials for Broadband Photodetectors," *Sci. Rep.*, vol. 10, no. 1, pp. 1–10, 2020, doi: 10.1038/s41598-020-63099-0.

[21] F. Xia, T. Mueller, Y. M. Lin, A. Valdes-Garcia, and P. Avouris, "Ultrafast graphene photodetector," *Nat. Nanotechnol.*, vol. 4, no. 12, pp. 839–843, 2009, doi: 10.1038/nnano.2009.292.

[22] J. Guo *et al.*, "High-performance silicon−graphene hybrid plasmonic waveguide photodetectors beyond 1.55 μm," *Light Sci. Appl.*, vol. 9, no. 1, 2020, doi: 10.1038/s41377-020-0263-6.

[23] V. Mišeikis *et al.*, "Ultrafast, Zero-Bias, Graphene Photodetectors with Polymeric Gate Dielectric on Passive Photonic Waveguides," *ACS Nano*, vol. 14, no. 9, pp. 11190–11204, 2020, doi: 10.1021/acsnano.0c02738.

[24] L. Zhuo *et al.*, "A broadband all-fiber integrated graphene photodetector with CNT-enhanced responsivity," *Nanoscale*, vol. 12, no. 26, pp. 14188–14193, 2020, doi:

10.1039/d0nr00139b.

[25] J. Gosciniak, M. Rasras, and J. B. Khurgin, “Ultrafast Plasmonic Graphene Photodetector Based on the Channel Photothermoelectric Effect,” *ACS Photonics*, vol. 7, no. 2, pp. 488–498, 2020, doi: 10.1021/acsphotonics.9b01585.

[26] G. Konstantatos *et al.*, “Hybrid graphene–quantum dot phototransistors with ultrahigh gain,” *Nat. Nanotechnol.*, vol. 7, no. 6, pp. 363–368, 2012, doi: 10.1038/nnano.2012.60.

[27] R. Pan *et al.*, “Excellent performance in vertical graphene-C60-graphene heterojunction phototransistors with a tunable bi-directionality,” *Carbon N. Y.*, vol. 162, pp. 375–381, 2020, doi: 10.1016/j.carbon.2020.02.030.

[28] J. Han *et al.*, “Light-modulated vertical heterojunction phototransistors with distinct logical photocurrents,” *Light Sci. Appl.*, vol. 9, no. 1, 2020, doi: 10.1038/s41377-020-00406-4.

[29] Z. Sun *et al.*, “Graphene mode-locked ultrafast laser,” *ACS Nano*, vol. 4, no. 2, pp. 803–810, 2010, doi: 10.1021/nn901703e.

[30] G. Yang, L. Li, and M. C. Ng, “Science and Technology of Advanced Materials Structure of graphene and its disorders: a review Structure of graphene and its disorders: a review,” 2018, doi: 10.1080/14686996.2018.1494493.

[31] M. I. Katsnelson, “The electronic structure of ideal graphene,” in *The Physics of Graphene*, Cambridge University Press, 2020, pp. 1–23.

[32] M. I. Katsnelson, “Graphene: carbon in two dimensions,” *Materials Today*, vol. 10, no. 1–2. Elsevier, pp. 20–27, Jan. 01, 2007, doi: 10.1016/S1369-7021(06)71788-6.

[33] H. Raza and E. C. Kan, “Armchair graphene nanoribbons: Electronic structure and electric-field modulation,” *Phys. Rev. B - Condens. Matter Mater. Phys.*, vol. 77, no. 24,

pp. 1–5, 2008, doi: 10.1103/PhysRevB.77.245434.

[34] V. P. Gusynin, V. A. Miransky, S. G. Sharapov, and I. A. Shovkovy, "Edge states, mass and spin gaps, and quantum Hall effect in graphene," *Phys. Rev. B - Condens. Matter Mater. Phys.*, vol. 77, no. 20, May 2008, doi: 10.1103/PhysRevB.77.205409.

[35] M. Zoghi, A. Y. Goharrizi, and M. Saremi, "Band Gap Tuning of Armchair Graphene Nanoribbons by Using Antidotes," *J. Electron. Mater.*, vol. 46, no. 1, pp. 340–346, 2017, doi: 10.1007/s11664-016-4940-4.

[36] Y. W. Son, M. L. Cohen, and S. G. Louie, "Energy gaps in graphene nanoribbons," *Phys. Rev. Lett.*, vol. 97, no. 21, pp. 1–4, 2006, doi: 10.1103/PhysRevLett.97.216803.

[37] G. Wang, "Effect of edge-hydrogen passivation and saturation on the carrier mobility of armchair graphene nanoribbons," *Chem. Phys. Lett.*, vol. 533, pp. 74–77, Apr. 2012, doi: 10.1016/j.cplett.2012.03.029.

[38] K. K. Jha, N. Tyagi, N. K. Jaiswal, and P. Srivastava, "Structural and electronic properties of armchair graphene nanoribbons functionalized with fluorine," *Phys. Lett. Sect. A Gen. At. Solid State Phys.*, vol. 383, no. 32, p. 125949, Nov. 2019, doi: 10.1016/j.physleta.2019.125949.

[39] C. Patel, R. Yogi, and N. K. Jaiswal, "First-principles study for I-V characteristics of halogen functionalized zigzag graphene nanoribbons," in *AIP Conference Proceedings*, Jul. 2019, vol. 2115, no. 1, p. 030451, doi: 10.1063/1.5113290.

[40] A. Kumar *et al.*, "Nitrogen-terminated semiconducting zigzag gnr fet with negative differential resistance," *IEEE Trans. Nanotechnol.*, vol. 13, no. 1, pp. 16–22, 2014, doi: 10.1109/TNANO.2013.2279035.

[41] B. Mandal, S. Sarkar, A. Pramanik, and P. Sarkar, "Electronic structure and transport

properties of sulfur-passivated graphene nanoribbons," *J. Appl. Phys.*, vol. 112, no. 11, 2012, doi: 10.1063/1.4768524.

[42] G. Lee and K. Cho, "Electronic structures of zigzag graphene nanoribbons with edge hydrogenation and oxidation," *Phys. Rev. B - Condens. Matter Mater. Phys.*, vol. 79, no. 16, pp. 20–24, 2009, doi: 10.1103/PhysRevB.79.165440.

[43] S.-M. Choi, S.-H. Jhi, and Y.-W. Son, "Effects of strain on electronic properties of graphene," 2010, doi: 10.1103/PhysRevB.81.081407.

[44] I. Y. Sahalianov, T. M. Radchenko, V. A. Tatarenko, G. Cuniberti, and Y. I. Prylutskyy, "Straintronics in graphene: Extra large electronic band gap induced by tensile and shear strains," *J. Appl. Phys.*, vol. 126, no. 5, Aug. 2019, doi: 10.1063/1.5095600.

[45] H. Liu, Y. Liu, and D. Zhu, "Chemical doping of graphene," *J. Mater. Chem.*, vol. 21, no. 10, pp. 3335–3345, Mar. 2011, doi: 10.1039/c0jm02922j.

[46] R. Deji, B. C. Choudhary, and R. K. Sharma, "Novel hydrogen cyanide gas sensor: A simulation study of graphene nanoribbon doped with boron and phosphorus," *Phys. E Low-dimensional Syst. Nanostructures*, vol. 134, p. 114844, Oct. 2021, doi: 10.1016/j.physe.2021.114844.

[47] V. Georgakilas *et al.*, "Functionalization of graphene: Covalent and non-covalent approaches, derivatives and applications," *Chem. Rev.*, vol. 112, no. 11, pp. 6156–6214, 2012, doi: 10.1021/cr3000412.

[48] V. Georgakilas *et al.*, "Functionalization of graphene: Covalent and non-covalent approaches, derivatives and applications," *Chemical Reviews*, vol. 112, no. 11. American Chemical Society, pp. 6156–6214, Nov. 14, 2012, doi: 10.1021/cr3000412.

[49] H. Zhang *et al.*, "Aryl functionalization as a route to band gap engineering in single layer

graphene devices," *Nano Lett.*, vol. 11, no. 10, pp. 4047–4051, Oct. 2011, doi: 10.1021/nl200803q.

[50] M. Di Giovannantonio *et al.*, "On-Surface Growth Dynamics of Graphene Nanoribbons: The Role of Halogen Functionalization," *ACS Nano*, vol. 12, no. 1, pp. 74–81, Jan. 2018, doi: 10.1021/acsnano.7b07077.

[51] S. Yang *et al.*, "A DFT study of CO adsorption on the pristine, defective, In-doped and Sb-doped graphene and the effect of applied electric field," *Appl. Surf. Sci.*, vol. 480, no. November 2018, pp. 205–211, 2019, doi: 10.1016/j.apsusc.2019.02.244.

[52] F. Chekin *et al.*, "MoS2/reduced graphene oxide as active hybrid material for the electrochemical detection of folic acid in human serum," *Biosens. Bioelectron.*, vol. 85, pp. 807–813, 2016, doi: 10.1016/j.bios.2016.05.095.

[53] P. K. Basu *et al.*, "Graphene based E. coli sensor on flexible acetate sheet," *Sensors Actuators, B Chem.*, vol. 190, pp. 342–347, 2014, doi: 10.1016/j.snb.2013.08.080.

[54] Y. H. Kwak *et al.*, "Flexible glucose sensor using CVD-grown graphene-based field effect transistor," *Biosens. Bioelectron.*, vol. 37, no. 1, pp. 82–87, 2012, doi: 10.1016/j.bios.2012.04.042.

[55] N. S. Green and M. L. Norton, "Interactions of DNA with graphene and sensing applications of graphene field-effect transistor devices: A review," *Anal. Chim. Acta*, vol. 853, no. 1, pp. 127–142, 2015, doi: 10.1016/j.aca.2014.10.023.

[56] L. Wu, L. Feng, J. Ren, and X. Qu, "Electrochemical detection of dopamine using porphyrin-functionalized graphene," *Biosens. Bioelectron.*, vol. 34, no. 1, pp. 57–62, Apr. 2012, doi: 10.1016/j.bios.2012.01.007.

[57] P. Singh, P. Abedini Sohi, and M. Kahrizi, "Finite Element Modelling of Bandgap

Engineered Graphene FET with the Application in Sensing Methanethiol Biomarker," *Sensors*, vol. 21, no. 2, p. 580, Jan. 2021, doi: 10.3390/s21020580.

[58] F. Schedin *et al.*, "Detection of individual gas molecules adsorbed on graphene," *Nat. Mater.*, vol. 6, no. 9, pp. 652–655, 2007, doi: 10.1038/nmat1967.

[59] B. Buszewski, D. Grzywinski, T. Ligor, T. Stacewicz, Z. Bielecki, and J. Wojtas, "Detection of volatile organic compounds as biomarkers in breath analysis by different analytical techniques," *Bioanalysis*, vol. 5, no. 18. Bioanalysis, pp. 2287–2306, Sep. 2013, doi: 10.4155/bio.13.183.

[60] K. E. van Keulen, M. E. Jansen, R. W. M. Schrauwen, J. J. Kolkman, and P. D. Siersema, "Volatile organic compounds in breath can serve as a non-invasive diagnostic biomarker for the detection of advanced adenomas and colorectal cancer," *Aliment. Pharmacol. Ther.*, vol. 51, no. 3, pp. 334–346, Feb. 2020, doi: 10.1111/apt.15622.

[61] J. Pawliszyn, "Development of SPME Devices and Coatings," in *Handbook of Solid Phase Microextraction*, Elsevier Inc., 2012, pp. 61–97.

[62] H. Chen, X. Qi, J. Ma, C. Zhang, H. Feng, and M. Yao, "Breath-borne VOC Biomarkers for COVID-19," *medRxiv*, p. 2020.06.21.20136523, Jan. 2020, doi: 10.1101/2020.06.21.20136523.

[63] I. H. Cho, D. H. Kim, and S. Park, "Electrochemical biosensors: Perspective on functional nanomaterials for on-site analysis," *Biomaterials Research*, vol. 24, no. 1. BioMed Central Ltd., pp. 1–12, Feb. 04, 2020, doi: 10.1186/s40824-019-0181-y.

[64] V. T. Le, Y. Vasseghian, E. N. Dragoi, M. Moradi, and A. Mousavi Khaneghah, "A review on graphene-based electrochemical sensor for mycotoxins detection," *Food Chem. Toxicol.*, vol. 148, p. 111931, Feb. 2021, doi: 10.1016/j.fct.2020.111931.

[65] J. Peña-Bahamonde, H. N. Nguyen, S. K. Fanourakis, and D. F. Rodrigues, "Recent advances in graphene-based biosensor technology with applications in life sciences," *Journal of Nanobiotechnology*, vol. 16, no. 1. BioMed Central Ltd., p. 75, Sep. 22, 2018, doi: 10.1186/s12951-018-0400-z.

[66] A. Agharazy Dormeny, P. Abedini Sohi, and M. Kahrizi, "Design and simulation of a refractive index sensor based on SPR and LSPR using gold nanostructures," *Results Phys.*, vol. 16, p. 102869, Mar. 2020, doi: 10.1016/j.rinp.2019.102869.

[67] P. A. Sohi and M. Kahrizi, "Principles and Applications of Nanoplasmonics in Biological and Chemical Sensing: A Review," in *Recent Advances in Nanophotonics - Fundamentals and Applications*, IntechOpen, 2020.

[68] Y. Bai, T. Xu, and X. Zhang, "Graphene-based biosensors for detection of biomarkers," *Micromachines*, vol. 11, no. 1. MDPI AG, Jan. 01, 2020, doi: 10.3390/mi11010060.

[69] M. B. Hossain, M. M. Rana, L. F. Abdulrazak, S. Mitra, and M. Rahman, "Graphene-MoS2 with TiO2[sbnd]SiO2 layers based surface plasmon resonance biosensor: Numerical development for formalin detection," *Biochem. Biophys. Reports*, vol. 18, p. 100639, Jul. 2019, doi: 10.1016/j.bbrep.2019.100639.

[70] Q. Wang, J. Y. Jing, and B. T. Wang, "Highly Sensitive SPR Biosensor Based on Graphene Oxide and Staphylococcal Protein A Co-Modified TFBG for Human IgG Detection," *IEEE Trans. Instrum. Meas.*, 2018, doi: 10.1109/TIM.2018.2875961.

[71] M. B. Hossain, M. M. Islam, L. F. Abdulrazak, M. M. Rana, T. B. A. Akib, and M. Hassan, "Graphene-Coated Optical Fiber SPR Biosensor for BRCA1 and BRCA2 Breast Cancer Biomarker Detection: a Numerical Design-Based Analysis," *Photonic Sensors*, vol. 10, no. 1, pp. 67–79, Mar. 2020, doi: 10.1007/s13320-019-0556-7.

[72] M. B. Hossain and M. M. Rana, “DNA Hybridization Detection Based on Resonance Frequency Readout in Graphene on Au SPR Biosensor,” *J. Sensors*, vol. 2016, 2016, doi: 10.1155/2016/6070742.

[73] M. K. Anvarifard, Z. Ramezani, and I. S. Amiri, “Label-free detection of DNA by a dielectric modulated armchair-graphene nanoribbon FET based biosensor in a dual-nanogap setup,” *Mater. Sci. Eng. C*, vol. 117, p. 111293, Dec. 2020, doi: 10.1016/j.msec.2020.111293.

[74] F. DJEFFAL, A. BENHAYA, K. TAMERSIT, and M. MEGUELLATI, “NEW DIELECTRIC MODULATED GRAPHENE (DMG) FETBASED SENSOR FOR HIGH-PERFORMANCE BIOMOLECULE SENSING APPLICATIONS,” Apr. 2015, pp. 401–414, doi: 10.1142/9789814667364_0030.

[75] G. Wadhwa and B. Raj, “Label Free Detection of Biomolecules Using Charge-Plasma-Based Gate Underlap Dielectric Modulated Junctionless TFET,” *J. Electron. Mater.*, vol. 47, no. 8, pp. 4683–4693, Aug. 2018, doi: 10.1007/s11664-018-6343-1.

[76] Ajay, R. Narang, M. Saxena, and M. Gupta, “Investigation of dielectric modulated (DM) double gate (DG) junctionless MOSFETs for application as a biosensors,” *Superlattices Microstruct.*, vol. 85, pp. 557–572, Jun. 2015, doi: 10.1016/j.spmi.2015.04.040.

[77] P. Singh, P. A. Sohi, and M. Kahrizi, “In silico design and analysis of Pt functionalized graphene-based FET sensor for COVID-19 biomarkers: A DFT coupled FEM study,” *Phys. E Low-dimensional Syst. Nanostructures*, vol. 135, no. April 2021, p. 114972, 2021, doi: 10.1016/j.physe.2021.114972.

[78] S. T. Epstein and C. M. Rosenthal, “The Hohenberg-Kohn theorem,” *J. Chem. Phys.*, vol. 64, no. 1, pp. 247–249, 1976, doi: 10.1063/1.431969.

[79] E. J. Bylaska, M. Holst, and J. H. Weare, “Adaptive finite element method for solving the exact kohn-sham equation of density functional theory,” *J. Chem. Theory Comput.*, vol. 5, no. 4, pp. 937–948, 2009, doi: 10.1021/ct800350j.

[80] J. P. Perdew, K. Burke, and M. Ernzerhof, “Generalized gradient approximation made simple,” *Phys. Rev. Lett.*, vol. 77, no. 18, pp. 3865–3868, 1996, doi: 10.1103/PhysRevLett.77.3865.

[81] M. Bokdam, P. A. Khomyakov, G. Brocks, and P. J. Kelly, “Field effect doping of graphene in metal|dielectric|graphene heterostructures: A model based upon first-principles calculations,” *Phys. Rev. B - Condens. Matter Mater. Phys.*, vol. 87, no. 7, pp. 1–13, 2013, doi: 10.1103/PhysRevB.87.075414.

[82] “Semiconductors,” in *Solid State Physics*, Berlin, Heidelberg: Springer Berlin Heidelberg, pp. 293–351.

[83] M. A. Green, “Intrinsic concentration, effective densities of states, and effective mass in silicon,” *J. Appl. Phys.*, vol. 67, no. 6, pp. 2944–2954, Mar. 1990, doi: 10.1063/1.345414.

[84] T. Gunst, T. Markussen, K. Stokbro, and M. Brandbyge, “First-principles method for electron-phonon coupling and electron mobility: Applications to two-dimensional materials,” *Phys. Rev. B*, vol. 93, no. 3, p. 035414, Jan. 2016, doi: 10.1103/PhysRevB.93.035414.

[85] K. Kaasbjerg, K. S. Thygesen, and K. W. Jacobsen, “Unraveling the acoustic electron-phonon interaction in graphene,” *Phys. Rev. B - Condens. Matter Mater. Phys.*, vol. 85, no. 16, p. 165440, Apr. 2012, doi: 10.1103/PhysRevB.85.165440.

[86] M. Bhattacharjee, N. Mandal, H. Nemade, and D. Bandyopadhyay, “Simulation of a Voltage Controlled Resistor Mimicking the Geometry of a MOSFET Device having

Graphite Channel," no. V, pp. 3–6, 2014.

[87] M. M. Montemore and J. W. Medlin, "A unified picture of adsorption on transition metals through different atoms," *J. Am. Chem. Soc.*, vol. 136, no. 26, pp. 9272–9275, 2014, doi: 10.1021/ja504193w.

[88] P. Singh, P. A. Sohi, and M. Kahrizi, "Effect of point defects in armchair graphene nanoribbons for biosensing of Methanethiol biomarkers: A DFT Study," *2021 IEEE 21st Int. Conf. Nanotechnol.*, pp. 142–145, Jul. 2021, doi: 10.1109/NANO51122.2021.9514321.

[89] "Methanethiol | CH3SH - PubChem." https://pubchem.ncbi.nlm.nih.gov/compound/methanethiol (accessed Oct. 07, 2020).

[90] G. K. Walia and D. K. K. Randhawa, "Adsorption and dissociation of sulfur-based toxic gas molecules on silicene nanoribbons: a quest for high-performance gas sensors and catalysts," *J. Mol. Model.*, vol. 24, no. 4, 2018, doi: 10.1007/s00894-018-3631-x.

[91] D. A. Neamen, "Semiconductor physics and devices : basic principles," p. 758, 2012.

[92] W. Zhou *et al.*, "Designing sub-10-nm Metal-Oxide-Semiconductor Field-Effect Transistors via Ballistic Transport and Disparate Effective Mass: The Case of Two-Dimensional Bi N," *Phys. Rev. Appl.*, vol. 13, no. 4, p. 1, 2020, doi: 10.1103/PhysRevApplied.13.044066.

[93] X. Gu and R. Yang, "First-principles prediction of phononic thermal conductivity of silicene: A comparison with graphene," *J. Appl. Phys.*, vol. 117, no. 2, p. 025102, Jan. 2015, doi: 10.1063/1.4905540.

[94] P. Van Mieghem, "Theory of Band Tails in Heavily Doped Semiconductors," *Rev. Mod. Phys.*, vol. 64, no. 3, pp. 755–792, 1992.

[95] P. A. Haddad, D. Flandre, and J. P. Raskin, “Intrinsic rectification in common-gated graphene field-effect transistors,” *Nano Energy*, vol. 43, no. October 2017, pp. 37–46, 2018, doi: 10.1016/j.nanoen.2017.10.049.